Resolving gas-phase metallicity in galaxies

Carton, D.J.

4

First gas-phase metallicity gradients of $0.1 \lesssim z \lesssim 0.8$ *galaxies with MUSE*

We present gas-phase metallicity gradients for 94 star-forming galaxies between $0.08 < z < 0.84$. We find a negative median metallicity gradient of $-0.043^{+0.009}_{-0.007}$ dex/kpc, i.e. on average we find the centres of these galaxies to be more metal-rich than their outskirts. However, there is significant scatter underlying this and we find that 10% (9) galaxies have significantly positive metallicity gradients, 39% (37) have significantly negative gradients, 28% (26) have gradients consistent with being flat, the remainder 23% (22) are considered to have unreliable gradient estimates. We find a slight trend for a more negative metallicity gradient with both increasing stellar mass and increasing star formation rate (SFR). However, given the potential redshift and size selection effects, we do not consider these trends to be significant. Indeed when we normalize the SFR of our galaxies relative to the main sequence, we do not observe any trend between the metallicity gradient and the normalized SFR. This finding is contrary to other recent studies of galaxies at similar and higher redshifts. We do, however, identify a novel trend between the metallicity gradient of a galaxy and its size. Small galaxies ($r_d < 3$ kpc) present a large spread in observed metallicity gradients (both negative and positive gradients). In contrast, we find no large galaxies ($r_d > 3$ kpc) with positive metallicity gradients, and overall there is less scatter in the metallicity gradient amongst the large galaxies. We suggest that these large (well-evolved) galaxies may be analogues of galaxies in the present-day Universe, which also present a common negative metallicity gradient.

David Carton, Jarle Brinchmann

1 Introduction

Gas is a key ingredient for star-formation in galaxies. Understanding how galaxies gain and lose gas is essential to explaining galaxy evolution. We know that now and in the past the gas reserves within galaxies are insufficient to sustain star-formation for long periods (Tacconi et al. 2013). Consequently we know that galaxies continue to acquire gas throughout their lives.

Metals provide a chemical tag that identifies the gas that has previously been associated with star-formation. Therefore by tracing the spatial distribution of gas-phase metallicity[1] throughout a galaxy we can learn how gas is recycled and redistributed within galaxies. Equally, we can also study how galaxies accrete and lose their gas.

In the classical inside-out picture of galaxy evolution, the inner regions of galaxies formed first from low angular momentum gas. And with the increase of angular momentum over time, radial scale-length of star-formation has progressed outwards in galaxies (Larson 1976). Inside-out growth can explain why the centre of the Milky Way is more metal-rich than its outskirts (Portinari & Chiosi 1999). Moreover it can also explain why exponentially-declining radial metallicity profiles are ubiquitous in isolated massive ($\gtrsim 10^8$ $M_\odot$) galaxies (e.g. Vila-Costas & Edmunds 1992; Zaritsky et al. 1994, and references therein).

More interestingly, not only do all star-forming galaxies present negative metallicity gradients, they present the same slope. That is, however, only once the metallicity gradient is normalized to the size of the galaxy (e.g. Sánchez et al. 2014; Ho et al. 2015). There is some debate over whether this trend continues into the outer disc of the galaxy. Indeed some have suggested that at large galactocentric radii the metallicity profile flattens (e.g. Rosales-Ortega et al. 2011; Bresolin et al. 2012; Marino et al. 2016), although it has also been suggested that the profile might steepen in the outer disc (Carton et al. 2015). Nevertheless the ubiquitous existence of a common metallicity gradient in the *inner discs* of galaxies is highly indicative of secular processes that dominate the growth of galaxies at late times.

Juxtaposed against this uniformity are observations of higher-redshift galaxies ($z \gtrsim 0.6$). Although on average metallicity gradients in these galaxies are flatter than today, there is a large amount of scatter (Stott et al. 2014; Wuyts et al. 2016). A common metallicity gradient does not exist in these galaxies. Strikingly, many high-redshift galaxies have positive (inverted) metallicity gradients (see e.g. Queyrel et al. 2012). Galaxies with centres more metal poor than their outskirts are rarely if ever observed in the present-day Universe.

The prevailing explanation for this phenomenon is that metal-poor gas is flowing (or has flowed) into the inner regions of these galaxies. The inflowing gas dilutes the metals, suppressing the metallicity. The acquisition of extra gas is subsequently expected to trigger intense star formation in the galaxy. In this regard Stott et al. (2014) identified a weak trend for elevated star-formation rates in the galaxies with flatter and inverted metallicity gradients.

There are two mechanisms that have been proposed to cause the inflow of metal-poor gas: galaxy–galaxy interactions and cold flows. Firstly, galaxy–galaxy interactions might trigger radial flows within a galaxy's disc, transporting metal-poor gas from the outskirts to the inner regions. There is observational support for this idea at low-redshift. Indeed, while it is true that there is a common metallicity gradient in isolated galaxies, non-isolated (interacting) galaxies possess significantly flatter metallicity gradients (Rich et al. 2012). Furthermore, this mechanism by which mergers flatten metallicity gradients has been demonstrated in numerical simulations (Rupke et al. 2010; Torrey et al. 2012). It appears, however, that galaxy–galaxy interactions are merely capable of flattening the metallicity gradient of galaxies, but not inverting it.

[1] Unless otherwise stated gas-phase metallicity (or simply metallicity) refers to the oxygen abundance ($12 + \log_{10}(\mathrm{O/H})$).

On the other hand, cold flows, the other mechanism proposed for producing inverted gradients, may be more successful (Cresci et al. 2010). These flows are cold streams of gas which can penetrate through a galaxies hot halo to reach the galaxy itself (Kereš et al. 2005; Dekel & Birnboim 2006). If this material follows the gravitational potential, it could dump metal-poor gas into the inner regions of galaxies. However, it has been suggested that instead these streams form a extended gas disc (Stewart et al. 2011; Danovich et al. 2015). The hypothesized cold-flows are expected to dominate the gas supply of a galaxy at early times ($z \gtrsim 1.8$), but are rarer at later times (van de Voort et al. 2011; Woods et al. 2014, e.g). So while cold flows may explain why at $z \approx 3.4$ observed galaxies present inverted gradients (Troncoso et al. 2014), it is harder to invoke cold flows to explain the inverted gradients at $z \approx 1$.

To summarize briefly, there is disparity between metallicity gradients in the high-redshift and low-redshift Universe. While not necessarily contradictory, the high-redshift results point to stochastic processes dominating galaxy evolution, while the low-redshift results suggest a secular evolution of galaxies. There are few or no observations of metallicity gradients in galaxies between $0.1 \lesssim z \lesssim 0.6$. Clearly, bridging this gap is a necessary step towards understanding the disparity between high and low redshift results. Here, with the Multi Unit Spectroscopic Explorer (MUSE; Bacon et al. (2010, and in prep.)), we will provide for the first time a large sample of metallicity gradients in intermediate-redshift galaxies ($0.08 < z < 0.84$).

Making these observations presents several challenges. The first challenge is to correct for the effects of seeing on our data. As demonstrated by Yuan et al. (2013), failing to correct for seeing effects will produce systemically flatter metallicity gradients. The challenge seeing poses is not unique to our work and other recent studies have used simulated observations to apply a-posteriori corrections to infer the true metallicity gradient. In Carton et al. (2017, herein Chapter 3) we presented an alternative forward-modelling approach. This method is better able to quantify the degeneracies that arise from seeing corrupted data, and therefore yields formal estimates for uncertainty in the recovered metallicity gradient.

A second challenge we face is that we derive metallicities from a combination of nebular emission-lines. Depending on a galaxy's redshift, different emission-lines fall within the wavelength range of a spectrograph. It is well-documented issue that different metallicity calibrations (especially when using different emission-lines) produce different results (e.g. Kewley & Ellison 2008). With our forward-modelling approach we can overcome these limitations and thereby self-consistently infer metallicity gradients independently of redshift.

With our observations of intermediate redshift galaxies we will attempt to reconcile the high and low-redshift pictures of galaxy evolution, particularly with respect to the gas-supply in these systems. We structure the paper as follows. In Section 2 we describe our observations our outline our galaxy selection and sample. We detail our methodology in Section 3, where we also include a sensitivity analysis for our model. Section 4 is dedicated to presenting the results on the derived metallicity gradients. In Section 5 we provide a discussion of these results. Finally we conclude our findings in Section 6.

Throughout the paper we assume a ΛCDM cosmology with $H_0 = 70\ \mathrm{km\,s^{-1}\,Mpc^{-1}}$, $\Omega_\mathrm{m} = 0.3$ and $\Omega_\Lambda = 0.7$.

2 Data

We wish to spatially resolve metallicity gradients in distant ($0.1 \lesssim z \lesssim 0.8$) galaxies. Using integral-field spectroscopy (IFS) we can map the nebular emission-lines emitted by star forming regions in these galaxies, and therefore measure radial metallicity variations.

Here we will use observations taken with the MUSE situated at UT4 of the Very Large Telescope (VLT). We will construct our galaxy sample by combining data from both Guaranteed

Time Observations (GTO) programmes and commissioning activities. However, because of the differing observing strategies employed in these observing campaigns, our data is rather inhomogeneous. Galaxies were observed with a variety of integration times (between 1 – 30 h) and in a variety of seeing conditions. We will describe these datasets fully in Section 2.1.2.

2.1 MUSE Observations

2.1.1 Instrument Description

MUSE is an integral-field spectrograph that employs an image slicing technique at optical wavelengths. In normal wide-field mode MUSE provides spectra over a continuous $1' \times 1'$ Field of View (FoV) with a continuous spectral coverage (4750Å – 9300Å). The spectra have a wavelength resolution of 2.3Å full-width half-maximum (FWHM). The spatial sampling of the data is $0.2'' \times 0.2''$, but the spatial resolution of our data is seeing-limited.

2.1.2 Field Description

Given MUSE's large contiguous field, we do not target individual galaxies, rather we target collections of galaxies with limited pre-selection. While each field was chosen to optimize the scientific objectives of the different observing programmes, in general the galaxy selection is essentially blind. There is one exception where one field (CGR28) targets a galaxy group at $z \approx 0.7$.

While the parent galaxy sample selection is essentially blind, there are no straightforward criteria for selecting the galaxies where we can measure metallicity gradients. That said we would expect that we can measure metallicity gradients in the largest and brightest galaxies at a given redshift. Therefore we do not make a-priori selection criteria, and analyse all MUSE detected galaxies that have known redshifts, rejecting those with insufficient signal-to-noise (S/N). We describe this S/N cut in Section 2.3.1. We present a post-hoc description of the final sample in Section 2.3.

We will now outline the data used in our analysis as follows (a summary is displayed in Table 4.1):

Hubble Deep Field South (HDFS) As one of the commissioning activities MUSE acquired a single deep field in the HDFS at a 26.5h depth (53×1800 s). The average seeing conditions were good (FWHM = $0.66''$ at 7000Å). Bacon et al. (2015) present a full description of the data. Here we use a slightly improved data reduction to the one presented therein. This new reduction includes improvements to the sky subtraction and slice normalization (quasi flat-fielding).

Hubble Ultra Deep Field (UDF) The MUSE-Deep GTO survey has observed a 9 field mosaic that covers the UDF. This $3' \times 3'$ field has been observed to a depth of ≈ 10 h (in exposures of 1500 s each). In addition, there is also an extra-deep $1' \times 1'$ portion of the mosaic that reaches ≈ 31 h. During the observations the average seeing conditions were good resulting in a PSF with FWHM = $0.61'' - 0.67''$ at 7000Å. This data will be appear in Bacon at al. (in prep.), the redshifts in Brinchmann et al. (in prep.) and the full catalogue with line fluxes etc. in Inami at al. (in prep.).

Chandra Deep Field South (CDFS) The MUSE-Wide GTO program is surveying a portion of the Chandra Deep Field South (amongst other fields). In the end this will produce a 60 tile mosaic of the CDFS at 1 h depth (using exposures of 4×900 s). Here we will use only the first 24 fields that have been observed. These observations were performed in moderate and

Table 4.1: Summary of galaxy observations. The final sample of galaxies were obtained from a various targeted fields (with differing exposure depths and seeing conditions). We list the number of galaxies obtained from each field.

Field	Depth [h]	PSF FWHM [arcsec]	# of galaxies in final sample
HDFS	26.5	0.66	12
UDF-Medium	≈ 10	0.61 – 0.67	33
UDF-Deep	≈ 31	0.65	9
CDFS	1	0.7 – 1.1	35
CGR28	9.75	0.60	4
CGR28-Snapshot	1	0.60	1

poor seeing conditions, resulting in a FWHM = 0.7″ – 1.1″ at 7000Å) This dataset will be described by Urrutia et al. (in prep.).

COSMOS Group 28 (CGR28) A third GTO program is surveying galaxies in group environments. In our analysis here we will use observations of one of these galaxy groups (namely Group 28 as identified in the zCOSMOS 20k Group Catalogue Knobel et al. (2012)). The deepest portion of the field is slightly less than the full 1′ × 1′ FoV and reaches a 9.75 h depth (39 × 900 s). However, due to none overlapping field pointings, a region at the field edge was only observed with 1 h depth. One galaxy (ID: 767296) in our final sample lies in this shallow region. The average seeing conditions were good (FWHM = 0.60″ at 7000Å). This field will be presented in Epinat et al. (in prep.).

2.1.3 Data Reduction

Above we described fields from four different observing programmes and as is to be expected, there are differences in the specifics for each of the data reductions. However, in common all reductions use the standard data reduction pipeline (Weilbacher, in prep.)[2] to produce calibrated datacubes. In all fields sky subtraction is performed using Zurich Atmospheric Purge (ZAP; Soto et al. (2016)) which employs a principal component analysis technique developed specifically for MUSE data.

The largest difference between the reductions are the implementations (or lack thereof) slice normalization. Slice[3] normalization improves the uniformity (flatness) of the field and are primarily required because the flat-field calibrations are not taken at the exact same time as the science exposures. Small changes in the instrument alignment due to thermal variations can alter the throughput to the slits. Slice normalization is essentially a secondary flat-fielding, that self-calibrates on the individual science exposures. Because multiple exposures are combined, these semi-random slice systematics contribute to the effective noise in the final datacube. The slice normalization is very important for faint galaxies, but will have little impact on the bright galaxies that we study here. Thus the fact that the various data reductions implement the normalization differently will not affect our results.

The final datacubes are constructed with equal sized voxels[4] (0.2″ × 0.2″ × 1.25Å), which mirrors the native pixel size at the charge-coupled device (CCD) level. With this voxel size, the typical seeing-limited point-spread function (PSF) is well sampled, whilst the 2.3Å line-spread function (LSF) is only just critically sampled.

[2] A short description of the pipeline can be found in Weilbacher et al. (2012)

[3] By slice we refer to the optical image slicers within MUSE, not the wavelength layers (channels).

[4] volumetric pixel

2.1.4 PSF Determination

A critical part of our analysis is to forward model the seeing effects on our data. It is therefore necessary to measure the final PSF directly from our datacubes. It is known that the MUSE PSF is relatively spatially invariant across the FoV, thus a PSF model fit to a bright star within the FoV can be applied across the whole field. Unfortunately, not all fields contain such bright stars, and therefore we use a variety of PSF determination techniques in the different fields:

HDFS This field contains a bright star to which Bacon et al. (2015) fit a Moffat function. The FWHM of the Moffat profile is allowed to vary as a function of wavelength, but the Moffat β parameter is not. We describe the FWHM as a piecewise linear function with three knots (at 4750, 7000, 9300Å).

UDF Some of the MUSE UDF pointings do not contain any bright stars. Thus the PSF must be inferred from non-point source objects (i.e. galaxies). Hubble Space Telescope (HST) images are convolved with the Moffat function and fit[5] to MUSE pseudo-broadband images. We obtain a best fit Moffat profile as a linear function of wavelength. The Moffat β parameter is assumed to be constant. The accuracy of this method has been verified by comparing the results in those fields that do contain bright stars.

CDFS As with the UDF, many of the CDFS fields are also devoid of bright stars. Here we use the brightest galaxies to measure the PSF. The shapes of these galaxies are measured using SExtractor (Bertin & Arnouts 1996). By modelling these sources as a 2D Gaussian, the best fit PSF for a series of MUSE pseudo-broadband images is found. This PSF is modelled as a Gaussian profile, where the FWHM varies linearly with wavelength. Fields that contain bright stars are also modelled with a direct fit to the star. These stellar fits are used if they indicate a FWHM that is a better match to the telescope autoguider measurements.

CGR28 This field contains four relatively faint stars. We perform a simultaneous fit to all stars using a Moffat PSF. The FWHM is assumed to have a 3$^{\text{rd}}$ order polynomial, whilst the Moffat β is assumed to only have a linear dependence.

To summarize, we model the PSF with an axisymmetric function (either a Moffat or Gaussian function). The FWHM is free to vary as function of wavelength, and is larger at bluer wavelengths. These wavelength-dependent PSF models are directly used in our forward-modelling of our observations.

2.2 Derived global properties

As part of our analysis we study metallicity gradients as a function of global galaxy properties, e.g. stellar mass, star formation rate, and disc size. We now outline how these quantities are derived.

2.2.1 Stellar Mass

There exists extensive broadband photometry for all of the fields that we study here. Stellar masses are estimated though stellar population synthesis (SPS) modelling. This yields a self-consistent mass estimate, despite the differing availability of filters in different fields. We use FAST (Kriek et al. 2009) to fit the photometry of each galaxy, using Bruzual & Charlot (2003) SPS models with a Chabrier (2003) initial mass function (IMF). We assume an exponentially declining star-formation history, SFR $= \exp(-t/\tau)$. The model grid is sampled in steps of 0.2 dex spanning $\log_{10}(t/\text{yr}) = [8.0, 10.2]$. The decay timescale is sampled in invervals

[5]The fit is performed in the Fourier space

of 0.5 dex covering $\log_{10}(\tau/\mathrm{yr}) = [8.5, 10.0]$. We include models with a range of *stellar* metallicities $Z = \{0.004, 0.008, 0.020, 0.050\}$. A Calzetti et al. (2000) dust law is assumed with V-band attenuations varied between $A_V = [0, 3]$ (in steps of 0.1 mag). We fix the redshift of the galaxy to that derived from the MUSE spectra.

Photometry used in each of the four fields is derived from various sources, all of which are approximations of the total magnitude:

HDFS For this field we use the four-band HST photometry {F300W, F450W, F606W, F814W} from Casertano et al. (2000).

UDF Extensive deep multi-band HST photometry is provied by Rafelski et al. (2015) in {F225W, F336W, F435W, F606W, F775W, F850LP, F105W, F125W, F140W, F160W}. Where possible, we use all filters.

CDFS Here we use the photometric catalogue of Guo et al. (2013) using exclusively the HST photometry {F606W, F775W, F814W, F850LP, F105W, F125W, F160W}, using all where available.

CGR28 In this field we adopt the photometric catalogue of Capak et al. (2007) using {Subaru $B_j\, V_j\, g^+\, r^+\, i^+\, z^+$ NB816, SDSS $u\, g\, r\, i\, z$, CFHT $u^*\, i^*$, HST F814W, CTIO/KPNO K_s}.

2.2.2 Star Formation Rate (SFR)

We derive global star formation rates directly from the MUSE data, taking the spectrum integrated across the whole galaxy. On this we perform a full spectral-fitting using PLATEFIT (Tremonti et al. 2004; Brinchmann et al. 2004). We will describe the spectral fitting in Section 3.1.2. Here is simply suffices to say that we obtain the Hα, Hβ and Hγ emission-line fluxes, accounting for the underlying stellar absorption.

For low-redshift galaxies ($z \lesssim 0.4$) we use Hα and Hβ to compute the SFR. At higher redshifts Hα is redshifted beyond the MUSE wavelength range, so we compute the SFR in these galaxies using Hβ and Hγ instead.

To correct for dust we adopt the Charlot & Fall (2000) birth-cloud absorption curve

$$L_{\mathrm{ext}}(\lambda) = L(\lambda) e^{-\tau(\lambda)}, \tag{4.1}$$

with

$$\tau(\lambda) = \tau_V \left(\frac{\lambda}{5500\,\text{Å}} \right)^{-1.3}, \tag{4.2}$$

where τ_V is the V-band optical depth. Depending on the redshift we use either the observed Hα/Hβ or Hγ/Hβ ratios to calculate τ_V. For this we assume intrinsic Case B Balmer recombination ratios of $j_{\mathrm{H}\alpha}/j_{\mathrm{H}\beta} = 2.86$ and $j_{\mathrm{H}\gamma}/j_{\mathrm{H}\beta} = 0.468$. These values are appropriate for H II regions of temperatures, $T_e = 10000\,\mathrm{K}$, and electron densities, $n_e = 100\,\mathrm{cm}^{-3}$ (Dopita & Sutherland 2003).

Finally, we convert dust corrected Hα luminosities to SFRs using a scaling relation between Hα and SFR

$$\log_{10}\left(\frac{\mathrm{SFR}}{\mathrm{M}_\odot\,\mathrm{yr}^{-1}} \right) = \log_{10}\left(\frac{L(\mathrm{H}\alpha)}{\mathrm{erg\,s}^{-1}} \right) - 41.27, \tag{4.3}$$

(Murphy et al. 2011; Hao et al. 2011; Kennicutt & Evans 2012).

2.2.3 Galaxy Morphology

In Chapter 3 we presented a method for modelling the metallicity gradients in our galaxies. As inputs, this method requires four basic morphological parameters describing: the galaxy centre (Right Ascension, RA, and Declination, Dec.), the inclination of the galaxy (inc.) and the position angle of the major axis on the sky (PA). For our discussion we also need galaxy size, which we shall express as the exponential disc scale-length, r_d.

All the fields we present here are well studied and have existing morphological catalogues.

HDFS For this field Contini et al. (2016) provide a detailed morphological analysis of the resolved galaxies. They perform a bulge-disc decomposition on the HST F814W imaging, which yields all the necessary morphology information.

UDF + CDFS For both these fields van der Wel et al. (2012) provide a catalogue of single Sérsic fits. While this catalogue provides most of the relevant information, it does not provide estimates for the galaxy inclinations. Instead it only provides the axis ratios of the galaxies. Since axis ratio is primarily a function of inclination, we can convert axis ratios into inclinations. However, axis ratios have a secondary dependence on the morphological type of the galaxy. Since the Sérsic index is a proxy for morphological type, we can reduce this secondary dependence by partitioning the catalogue into quintile bins of the Sérsic index. Within each of the these bins we order the galaxies by decreasing axis-ratio. Since we view galaxies from orientations, we assume this order represents a linear sequence of increasing galaxy inclination between $[0° - 90°]$. We can use the rank order of the galaxy within the bin to estimate its inclination.
To estimate the galaxy sizes we use the half-light radii, r_e, reported in the catalogue. To convert these to disc scale-lengths we simply assume that the galaxy profile is a bulgeless exponential disc (i.e. $r_d \approx 0.596\, r_e$).
The catalogue provides the morphology derived from three HST bands (F105W, F125W and F160W). For any given galaxy we use the morphology of the band with the highest S/N.

CGR28 For this field we use the morphological assessment provided by the COSMOS 2005 Morphology Catalogue, which uses MORPHEUS (Abraham et al. 2007) to measure the morphological parameters. As above, this catalogue also only reports a galaxy's axis ratio, not inclination. Again we apply the rank ordering method to convert to axis ratio into a inclination. To avoid mixing morphological types, we use the concentration index as a proxy for morphological type. We divide the catalogue into decile bins of the concentration index, and perform the rank ordering within each. This catalogue provides the half-light radii of the galaxies, which we convert to exponential disc scale-lengths as above.

The galaxy morphology from the different catalogues are measured in different photometric bands. This will systematically affect the measured galaxy sizes. Sizes of late-type galaxies measured at redder rest-frame wavelengths will appear systematically smaller. To correct for this we use the parametrization of van der Wel et al. (2014) (their equations 1 & 2). This correction depends only on the galaxy's redshift and stellar mass. In this work all galaxy sizes are quoted as if they were measured at a rest-frame wavelength of 5000Å.

2.3 Sample Description

As mentioned previously, we do not make an a-priori selection for our sample. Nevertheless, there are many galaxies for which we cannot meaningfully constrain the metallicity gradient. Naturally we would expect we can only measure metallicity gradients in the largest and brightest galaxies. However, it is non-trivial to map this to a clean cut on global properties

(e.g. stellar mass, size and SFR). Therefore we build our final sample based upon data-driven criteria (i.e. S/N).

2.3.1 Selection Criteria

We extract spatially resolved emission-line fluxes from our parent sample of 590 MUSE detected galaxies (with $z < 0.85$). The procedure for this extraction is described in Section 3.1. In many galaxies we fail to detect any emission-line component.

To meaningfully constrain metallicity (and distinguish its effects from dust) we need two strong forbidden lines and two Balmer lines to be detected at S/N $\geq$ 5. Exactly which emission lines are chosen depends on the galaxy. Using the globally integrated spectrum we choose the two forbidden lines with the highest S/N, and the two Balmer lines with the highest S/N. A typical emission-line choice for a low-redshift galaxy might be {Hβ, [O III]5007, Hα, [S II]6717,6731}. And a typical choice at high-redshift might be {[O II]3726,3729, Hγ, Hβ, [O III]5007}.

Since we need to constrain the metallicity gradient of the galaxy, not just its metallicity, the line emission must be detected in multiple spatial bins. Explicitly we require that the four chosen emission-lines are all detected at S/N $\geq$ 5 in at least three spatial bins. (The spatial binning scheme is described in Section 3.1.1).

Overall these criteria amount to a minimum S/N cut. How this selection maps to galaxy properties depends on the field (because our observations have different depths and seeing conditions).

In addition to this main selection cut, we apply three further criteria:

- Rarely, but on occasion, the emission we detect may not be associated with the target of interest, i.e. the data is contaminated by a brighter neighbouring galaxy, at the same redshift. These cases can be identified through visual inspection. We manually excluded galaxies where contamination is apparent.

- When modelling the metallicity gradients in our galaxies we assume the galaxies infinitesimally thin disc. This approximation is acceptable for face-on galaxies, however, it becomes increasingly questionable for more inclined systems. We therefore exclude galaxies with an estimated inclination inc. $> 70°$.

- Galaxies with bright active galactic nuclei (AGN) will produce bright line-emission. Such emission would alter the observed emission-line ratios, and thus alter the inferred metallicities. In the following section we explain how we exclude AGN.

2.3.2 AGN Exclusion

It is difficult to determine the metallicity of galaxies when they are contaminated by emission from AGN or low-ionization nuclear emission-line regions (LINERs). We could treat such galaxies in one of three ways. Firstly one could attempt to model the flux contribution from a compact central source. Secondly we could mask out the central regions of a galaxy, and derive the metallicity gradient from the outer regions of the galaxies. A third approach, and the one we adopt here, is to simply discard galaxies from our sample if they appear to have a significant AGN/LINER component. We classify our galaxies using standard emission-line ratios classifications, which we apply to a galaxy's globally integrated spectrum.

At low redshift ($z \lesssim 0.4$) we use the both [N II]/Hα and [O III]/Hβ ratios to classify galaxies. We follow the classification scheme of Brinchmann et al. (2004) to divide galaxies into three categories: pure star forming, those with significant AGN, and those that fall in between (i.e.

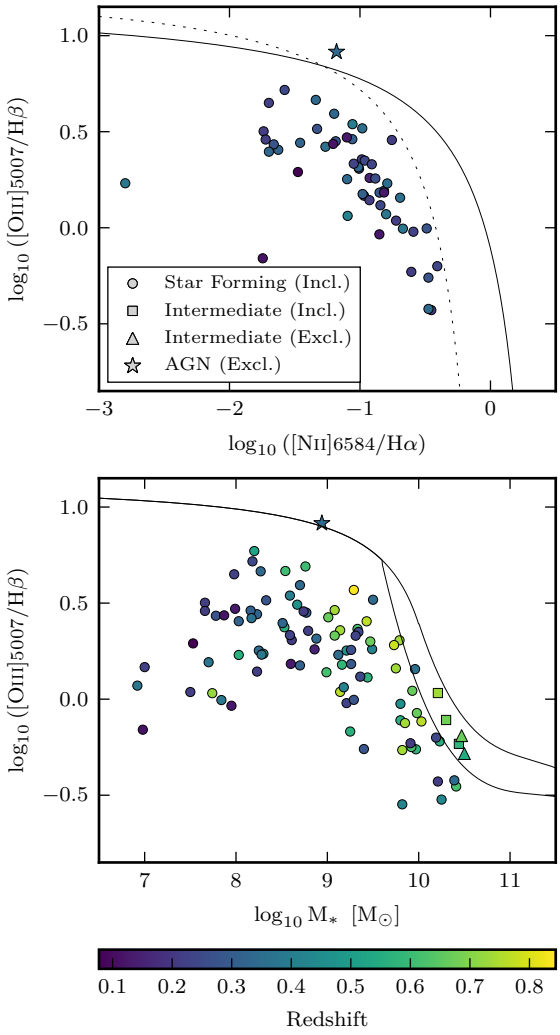

Figure 4.1: Diagnostic plots for AGN classification. Our final sample of star forming galaxies and included intermediate galaxies are plotted as circles and squares, respectively. Excluded intermediate and AGN/LINER galaxies are indicated by triangles and stars, respectively. Data points are colour coded by redshift. (Left) We plot [N II]/Hα versus [O III]/Hβ diagnostic (a BPT (Baldwin et al. 1981) diagram) for the low redshift ($z \lesssim 0.4$) portion of our sample. As a solid line we indicate the Kewley et al. (2001) theoretical maximum limit for star formation alone. With a dashed line we show the Kauffmann et al. (2003) curve, the empirical division between emission from star formation and AGN/LINER emission. (Right) We show the Mass-Excitation (MEx) diagram for our sample, including also the Juneau et al. (2014) demarcations as solid black lines. Note that galaxies which appear on left (the BPT diagram) also appear the right (the MEx diagram).

intermediate). We exclude galaxies classified as AGN, but we do not automatically exclude the intermediate cases. These intermediate galaxies are inspected manually and we exclude those that possess broad emission-line velocity components, indicative of AGN.

At $z \gtrsim 0.4$ the [N II]/Hα is redshifted out of MUSE's wavelength range. Therefore we adopt the Mass-Excitation (MEx) diagnostic (Juneau et al. 2014) to classify the galaxies into the same three classifications (star forming, intermediate, AGN). As before intermediate cases are manually inspected.

In Fig. 4.1 we show where our galaxies lie with respect to the two diagnostics. Out of 97 galaxies we exclude one galaxy below $z \approx 0.4$ and two galaxies above.

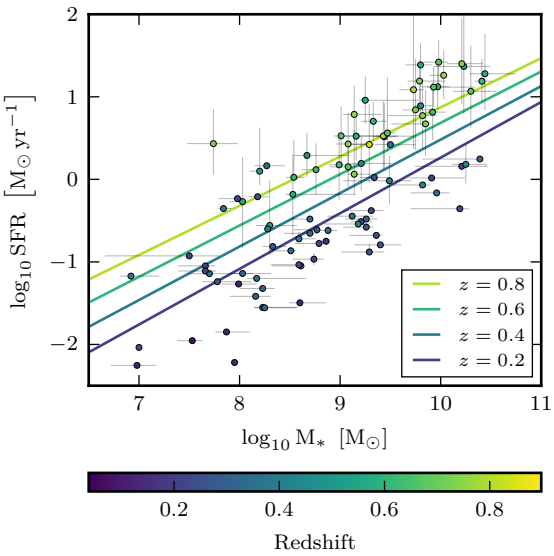

Figure 4.2: Mass versus SFR for our final sample plotted as coloured circles. For comparison, we display the main sequence at four different redshifts as solid lines, adopting the parametrization of Whitaker et al. (2012). Note that the SFR of the low redshift galaxies are derived from Hα and Hβ lines, whilst the high redshift galaxies are derived from Hβ and faint Hγ lines. Consequently the SFR errors are much smaller for the low redshift galaxies.

2.3.3 Sample Properties

In Fig. 4.3 we present the global properties of our final sample. Therein we show the distributions of stellar mass, SFR, rest frame B–V colour and main-sequence offset (ΔSFR)[6] In addition and for comparison we also plot the parent sample of MUSE galaxies. This includes all galaxies, even those that do not meet our selection criteria (Section 2.3.1).

In can clearly be seen that our final sample preferentially selects the more massive and more strongly star forming galaxies. There is also a clear redshift dependence such that in panel (a) the low-mass are almost exclusively low-redshift galaxies. Similar is true for the SFR (panel b), where the effect appears even stronger.

In contrast, both B–V colour and ΔSFR show different trends. In panel (c) we see that below (B–V) $\lesssim 0.6$ mag our final sample is fairly representative of the parent sample. We note that the galaxy redshifts are relatively evenly distributed between each bin.

Similar is true for the main-sequence offset parameter (panel d) where, above $\Delta\text{SFR} \gtrsim 0$ dex, the final sample traces the same shape of the parent sample. Above the main-sequence ($\Delta\text{SFR} > 0$ dex) the redshifts are also evenly distributed. We can display this another way; in Fig. 4.2 we show the mass–SFR correlation for our galaxies. At high-redshift our galaxies all lie above or on the main-sequence. And at low-redshift a large fraction of galaxies are found below the main-sequence.

To summarize, while at high redshift we are biased towards massive, strongly star-forming galaxies, at all epochs we are selecting blue galaxies that lie on the upper-half of the main sequence.

[6] We define ΔSFR to be the difference in the observed SFR relative to what would be expected for a galaxy on the main-sequence, with the same stellar mass and at the same redshift. Here and throughout this paper we adopt the main sequence as that parametrized by Whitaker et al. (2012).

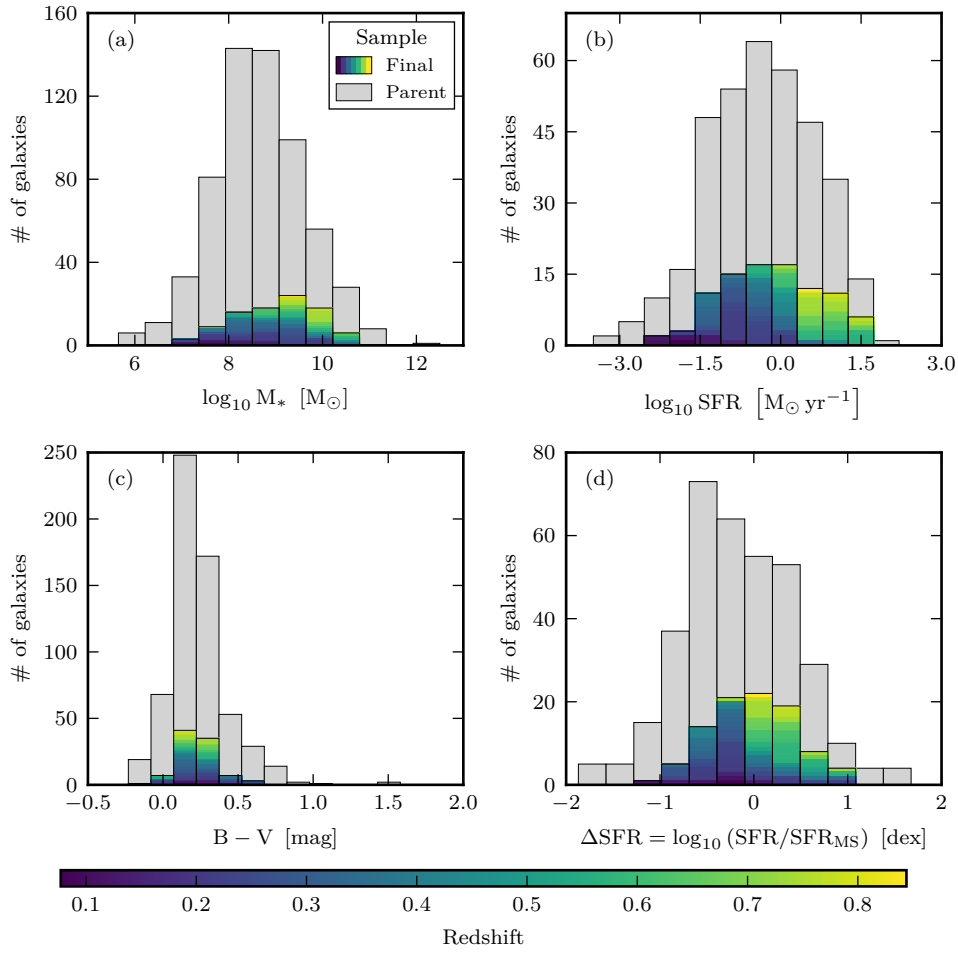

Figure 4.3: The distributions of various global galaxy properties of our final sample are shown as coloured histograms. The grey histograms show the distribution of galaxies from the parent sample. Galaxies in the final sample are coloured by their redshift. If the histogram bins were independent of redshift then each bin would be similarly coloured. We show four properties: (a) stellar mass, (b) star-formation rate, (c) rest frame Bessel B–V colour and (d) offset from the star-forming main sequence, accounting for redshift evolution. Rest frame colours are determined from the best-fit FAST spectrum to the photometry (see Section 2.2.1). While most galaxies in the parent sample have reliable photometry allowing us to derive masses and colours, fewer galaxies in the parent sample have detected line-emission. Consequently there are fewer galaxies in the parent sample in panels (b & d).

3 Analysis

Many of the galaxies are heavily corrupted by seeing. Additionally we further lose resolution when we aggregate (or "bin") spaxels[7] together. Binning spaxels is essential for increasing the S/N in our data. So, to recover the intrinsic metallicity gradient in our galaxies, we must model both the effect of seeing and binning on our data.

In Chapter 3 we demonstrated such a method for inferring both the central metallicity, $\log_{10} Z_0$, and metallicity gradients, $\nabla_r (\log_{10} Z)$ in distant galaxies. In this paper we now apply this method to a sample of galaxies observed with MUSE. We have made a few minor modifications to the method presented in Chapter 3. For brevity here we only describe the method in outline.

In the next section we will first explain how we extract the emission line fluxes (Section 3.1). We will then proceed to describe the fitting of our model to the data (Section 3.2). Finally we shall demonstrate how sensitive our recovered model parameters are to particular model inputs (Section 3.3).

3.1 Emission line flux extraction

When extracting emission-line fluxes there is a trade off between the number of spatial bins and the S/N of the data within each bin. One must choose a S/N threshold that is sufficiently high to minimize systematic errors in the emission-line measurements, whilst avoiding losing too much spatial information.

3.1.1 Spatial Binning

In Chapter 3 (appendix C) we designed a binning algorithm that attempts to maximize the number of spatial bins above a S/N threshold. In essence this algorithm performs successive passes over the data where, on each iteration, the bin size is increased.

When calculating the S/N of a bin, we perform a full spectral fitting to the coadded spectrum. A successful bin must have all emission-lines with S/N ≥ 5, where set of tested emission-lines is chosen on an object-by-object basis. This set typically consists of four lines, the two highest S/N Balmer lines and two highest S/N forbidden lines.

There are some oddities that arise from our binning strategy. To preserve radial information we define our spatial bins in polar coordinates (in a plane inclined to the observer). As a direct consequence of working in a non-Cartesian coordinate system, the pixels within a bin are not necessarily all close to each other in Cartesian space. An addition oddity is caused by the successive passes with increasing bin size. This can result with bins that are (partially or entirely) enclosed within another. While neither of these effects are ideal, we remind the reader that we mirror the exact binning in the model (the segmentation map, which is the same for all emission lines, is a model input).

Finally we note that, because we do not impose a minimum bin size, our spatial bins can be much smaller than the PSF. Consequently emission-line fluxes of adjacent bins are not strictly statistically-independent.

3.1.2 Spectral Fitting

To extract the emission-line fluxes from the MUSE spectra we use the PLATEFIT spectral fitting code (Tremonti et al. 2004; Brinchmann et al. 2004). PLATEFIT applies a two-step process that first fits the stellar continuum (with emission-lines masked) before fitting the nebular

[7] spatial pixels

emission-line component (with the best-fit continuum subtracted). Note that the procedure we employ here is identical to that presented in Chapter 3 (section 4.2). Nevertheless we shall summarize it briefly here.

The continuum fitting step of PLATEFIT is not able to fit either the redshift or velocity dispersion of the spectrum. These two parameters must be provided in advance, and we do so as follows. The redshift of the spectrum is obtained using AUTOZ (Baldry et al. 2014). We wish this to be robust, so if value determined by AUTOZ deviates by more than $\pm 500\,\mathrm{km\,s^{-1}}$ from our initial redshift guess we default to that initial value. To estimate the velocity dispersion we use VDISPFIT[8]. At low S/N, however, VDISPFIT can yield outliers beyond the range $[10 - 300]\,\mathrm{km\,s^{-1}}$. If values outside this range are produced, we adopt a default value of $80\,\mathrm{km\,s^{-1}}$.

With the values of the redshift and velocity dispersion predetermined, the stellar continuum is fit using a combination of Bruzual & Charlot (2003) SPS model templates. If the continuum fitting fails (because the stellar continuum is too faint or non-existent) we estimate the continuum using a running median filter (width 150Å).

In the second PLATEFIT step the best fit continuum is subtracted from the observed spectrum. The emission lines are modelled as Gaussian functions. The velocity offset and velocity dispersions are the same for all emission lines. However, unlike the continuum fitting, these two velocity components are free parameters and need not be specified in advance.

The emission-line fluxes are determined from the spectral fitting, however, the formal emission-line flux errors are typically underestimated (see Brinchmann et al. 2013). We rescale these formal errors using a S/N dependent correction to obtain better estimates of the true flux error. The correction factors for this were determined from duplicate Sloan Digital Sky Survey (SDSS; York et al. (2000)) observations. Note that the SDSS spectra are of resolution comparable to MUSE.

3.2 Inferring metallicities

In Chapter 3 (section 2) we described our method for modelling the 2D emission-line flux distribution of galaxies and how this is fit to our observations. The galaxy is approximated as an infinitesimally thin disc, inclined to the observer. The disc is described by four fixed morphological parameters (RA, Dec, inc., PA). Our model contains five free parameters: total SFR of the galaxy, $\mathrm{SFR_{tot}}$, central metallicity, $\log_{10} Z_0$, metallicity gradient $\nabla_r (\log_{10} Z)$, ionization parameter at solar metallicity, $\log_{10} U_\odot$, and the V-band optical depth, τ_V.

The metallicity profile in the galaxy is axisymmetric and is described by an exponential function

$$\log_{10} Z(r) = \nabla_r (\log_{10} Z)\, r + \log_{10} Z_0, \tag{4.4}$$

where r is the radius.

We assume the ionization parameter is anti-correlated with metallicity following

$$\log_{10} U\,(Z) = -0.8 \log_{10} (Z/Z_\odot) + \log_{10} U_\odot, \tag{4.5}$$

where $Z_\odot$ is solar abundance and $\log_{10} U_\odot$ is the ionization parameter at solar abundance.

To predict the observed emission-line ratios we use the photoionization models of Dopita et al. (2013, herein D13) . At each spatial position we interpolate the model grids with the appropriate values of metallicity and ionization parameter. The modelled emission-line *ratios* only depend on the radial coordinate; there is no azimuthal dependence.

We wish to include the Hδ and Hϵ emission lines in our model fit. However, these Balmer lines are not provided by the D13 photoionization models. To include these lines

[8] http://spectro.princeton.edu/idlspec2d_install.html

we need to extend the D13 photoionization models. We do this by tabulating the Case B recombination ratios $j_{H\delta}/j_{H\beta}$ and $j_{H\epsilon}/j_{H\beta}$ as a function of $j_{H\gamma}/j_{H\beta}$. By interpolating these at the D13 photoionization model values of $L_{H\gamma}/L_{H\beta}$, we assign the appropriate $L_{H\delta}$ and $L_{H\epsilon}$ for each photoionization model. The Case B recombination ratios were determined with PyNeb (Luridiana et al. 2015) using atomic data from Storey & Hummer (1995).

3.2.1 SFR Maps

To model the emission-line *luminosities* we need to model the SFR distribution in the galaxy. For this one could adopt a parametric model, for example Wuyts et al. (2016) assume an exponential disc (SFR declines exponentially with increasing radius). However, since we have high-resolution HST imaging for all our galaxies, we prefer to relax this assumption and provide a 2D SFR map. Unlike the emission-line *ratios*, the modelled emission-line *luminosities* do have an azimuthal dependence.

Using the HST images we assume the distribution of stellar light provides a rough approximation for the relative SFR distribution. In the MUSE-Deep UDF fields we use the deep HST F775W imaging. In all other fields we use the F814W band which is close in wavelength. To ensure a consistent approach, we choose to use the F775W and F814W filters, which are similar in pivot-wavelength. These filters also have good S/N in all fields.

We construct SFR maps of our galaxies by cropping the HST images to only include flux within an ellipse of radius $4 \times r_d$. This ellipse has the same morphology (RA, Dec, inc., PA) as above. We inspect each image and alter the mask if necessary to ensure that we include all flux from the object and to remove other objects or defects. When necessary we interpolate over these rather than mask them. Negative flux values are set to zero. The final result is an SFR map that represents the *relative* spatial distribution of the SFR. The absolute SFR values are determined by normalizing the map to the total SFR, SFR_{tot}, which is a free parameter in the model.

3.2.2 Model Fitting

With this galaxy model we are able to mimic the resolution loss due to the seeing and spatial binning. Thus for every spatial bin we can generate a set of model fluxes that can be compared to those observed.

We fit emission lines that are observed at S/N ≥ 5[9]. For clarity, we emphasize that this is all emission-lines, not just the four chosen in Section 2.3.1. In other words, some emission-lines may only be detected in a few bins, but a critical subset (two Balmer, two forbidden) will be detected in all bins.

To fit our model to the data we use the MultiNest multi-modal nested sampling algorithm (Feroz et al. 2009; Feroz & Hobson 2008; Feroz et al. 2013) that we access through a Python wrapper (Buchner et al. 2014). With MultiNest we can calculate the posterior probability distributions (posteriors) of our five model parameters.

The prior probability distributions (priors) that we place on our model parameters are outlined in Table 4.2. Except for two differences, these priors are mostly similar to the priors that were adopted in Chapter 3.

One difference is that we now adopt a logarithmic prior on SFR_{tot}, where previously (for technical reasons) we had adopted a linear prior between $[0, 100]$ $M_\odot yr^{-1}$. For a normalization parameter we believe that a logarithmic prior is more appropriate. Changing this prior should

[9] We fit [O II]3726, [O II]3729, [O II]3726,3729, [Ne III]3869, Hϵ, Hδ, Hγ, Hβ, [O III]4959, [O III]5007, [N II]6548, Hα, [N II]6584, [S II]6717, [S II]6731 and [S II]6717,6731. We exclude redundant lines, i.e. if [O II]3726,3729 is detected at S/N ≥ 5, then we do not also fit [O II]3726 and [O II]3729.

Table 4.2: Priors on model parameters. For each parameter we detail the type of prior and the range of values covered.

Parameter	Prior type	Range
SFR_{tot}	Logarithmic	$[0.01, 100]\ M_{\odot} yr^{-1}$
$\log_{10} Z_0$	Linear	$\approx [-1.30, 0.70]$ dex
$\nabla_r (\log_{10} Z)$	Linear	$[-0.3, 0.3]$ dex/kpc
$\log_{10} U_{\odot}$	Linear	$\approx [-5.02, -1.42]$ dex
τ_V	Linear	$[0, 4]$

have little effect on the derived metallicity profiles, provided that the dust attention, τ_V, is well constrained by the data.

A second and more significant change is that we now adopt a narrower prior on the metallicity gradient, $\nabla_r (\log_{10} Z)$ (previously we had adopted $[-0.5, 0.5]$ dex/kpc). In Chapter 3 (appendix B) we identified that the inferred metallicity gradients could be sensitive to the choice of prior. We attributed this sensitivity to the finite range of metallicities spanned by the photoionization model grid. Metallicity profiles of galaxies with low central metallicities and a steep negative metallicity gradients will bottom-out at the lowest metallicity allowed by the photoionization model grid. As a direct result, negative metallicity gradients become somewhat degenerate in models with low central metallicities. Likewise, positive metallicity gradients become degenerate in models with high central metallicities.

In Chapter 3 we found that allowing an unnecessarily broad range of metallicity gradients could skew our inferences towards extreme values of the metallicity gradient. Hence we have now chosen to limit our metallicity gradient prior to the range $[-0.3, 0.3]$ dex/kpc. This spans the variety of currently measured metallicity gradients (e.g. Marino et al. 2016; Wuyts et al. 2016; Leethochawalit et al. 2016). In the following section we will assess the sensitivity of our results to various parameters, including the width of this prior.

3.3 Sensitivity analysis

With our model we perform fit with five free parameters. However, in our modelling we make particular choices, and fix certain parameters. We should attempt to assess the sensitivity of our results to these, considering both the magnitude of systematic errors we could expect, and the significance of unaccounted random uncertainties.

Here we will investigate four possible sources of additional errors: the width of the metallicity gradient prior, a misestimation of the PSF, a miscalculation the galaxy's inclination, and a misidentification of the galaxy centre. To estimate the size of these effects we re-analyse our galaxies, altering one of the parameters (e.g. increasing the FWHM of the PSF by 10%). By comparing the difference between this alternate model and the fiducial model, we can assess the impact of unaccounted systematics.

3.3.1 Sensitivity to the width of metallicity gradient prior

First we wish to identify the galaxies that are sensitive to the choice in metallicity gradient prior. In Fig. 4.4(a) we compare the differences between two flat priors with different widths: $[-0.3, 0.3]$ (our fiducial prior) and $[-0.5, 0.5]$ dex/kpc (the alternate prior). We see that most galaxies lie on the 1:1 line indicating that they are robust against the choice of prior. However, we note that some galaxies deviate significantly, showing a high degree of sensitivity to the prior. This sensitivity to the prior indicates an unreliable estimate of the metallicity gradient.

These galaxies should be treated with care in any analysis.

To assess this sensitivity we need a metric to quantify the difference between the fiducial and alternate models. For this we use the Jensen–Shannon distance applied to the metallicity gradient posteriors derived from the two models

$$\mathrm{JS}_{\mathrm{dist}} = \sqrt{\frac{1}{2}\sum_i P_i \ln\frac{P_i}{Q_i} + \frac{1}{2}\sum_i Q_i \ln\frac{Q_i}{P_i}}, \tag{4.6}$$

where P_i and Q_i are the discretized posteriors of the fiducial and alternate models, respectively. We place an arbitrary cut on galaxies with large Jensen–Shannon distances ($\mathrm{JS}_{\mathrm{dist}} > 0.3$). From Fig. 4.4(a) this can be seen to be a good identifier of galaxies deviating from the 1:1 line. In the remainder of this work we consider the derived metallicity gradients for these galaxies to be suspect, and we will flag them as potentially unreliable. For transparency we do not discard them and, unless otherwise stated, we include them in our statistics.

3.3.2 Sensitivity to PSF errors

The assumed PSF is perhaps one of the greatest sources of unaccounted error in our analysis. In our model we assume to know the PSF perfectly, however, the true PSF is somewhat uncertain, particularly in the fields that do not contain bright stars. Uncertainties in the PSF lead to additional random errors in our result. But more severely, if we incorrectly parametrize the PSF, we could systematically bias our inferred metallicity gradients.

While it is challenging to truly characterize the effects of PSF errors, we can nevertheless attempt to estimate the magnitude of the problem. To do this we re-analyse our galaxies adopting two different PSF, one where the FWHM is systemically 10% smaller than the fiducial model, and another where it is 10% larger. We show the latter case in Fig. 4.4(b) and, as is to be expected, if we overestimate the PSF width then we will systematically overcorrect for seeing effects and infer systemically steeper metallicity gradients.

There is also noticeable scatter, a moderate uncertainty in the PSF will displace some galaxies significantly from the 1:1 line. In general, we find that the smaller galaxies are most sensitive. We can use the vertical displacement from the 1:1 line as indication of the expected additional uncertainly. We calculate the standard deviation (weighted by the inverse of the mean $1\,\sigma$ error), and find the additional uncertainty to be $\approx 0.03\,\mathrm{dex/kpc}$. This estimate is the mean uncertainty averaging the two alternative models where the PSF is 10% smaller and 10% larger. Naturally this value is only indicative and should not be treated as exact. Not least because it will vary from galaxy to galaxy.

3.3.3 Sensitivity to galaxy inclination errors

Another possible source of uncertainty is the inclination of the galaxy. Whilst it is not so likely that we systematically miscalculate the inclination, there is certainly some random error. In general inclination is most uncertain for face-on galaxies, however, this is counteracted by the fact that the metallicity gradient derived from face-on galaxies are probably the most robust against errors in the inclination.

As a rough guess we consider inclination uncertainties of the order $\pm 10°$ and construct two alternate models. We show one of these models in Fig. 4.4(c). This plot indicates that if we overestimate the inclination we will derive systematically smaller metallicity gradients. However, we note that most galaxies have small Jensen–Shannon distances and clearly lie on the 1:1 line (with minimal scatter). This would indicate that in general our model is robust against inclination uncertainties. As before, from the vertical scatter we estimate the additional uncertainty to be $\approx 0.01\,\mathrm{dex/kpc}$.

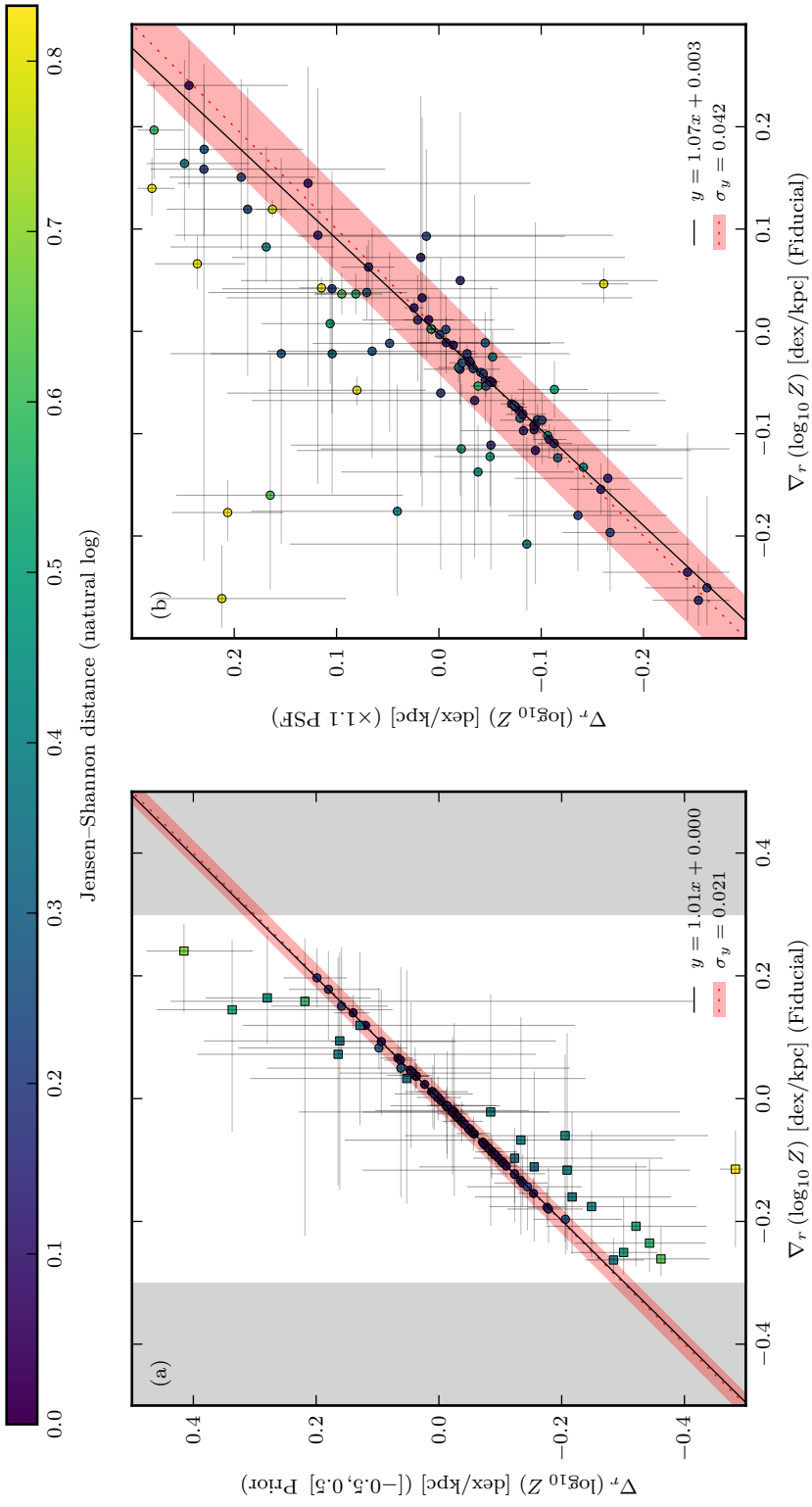
(a)
(b)
$y = 1.01x + 0.000$
$\sigma_y = 0.021$
$y = 1.07x + 0.003$
$\sigma_y = 0.042$
∇_r ($\log_{10} Z$) [dex/kpc] ([−0.5, 0.5] Prior)
∇_r ($\log_{10} Z$) [dex/kpc] (×1.1 PSF)
∇_r ($\log_{10} Z$) [dex/kpc] (Fiducial)
∇_r ($\log_{10} Z$) [dex/kpc] (Fiducial)
Jensen–Shannon distance (natural log)

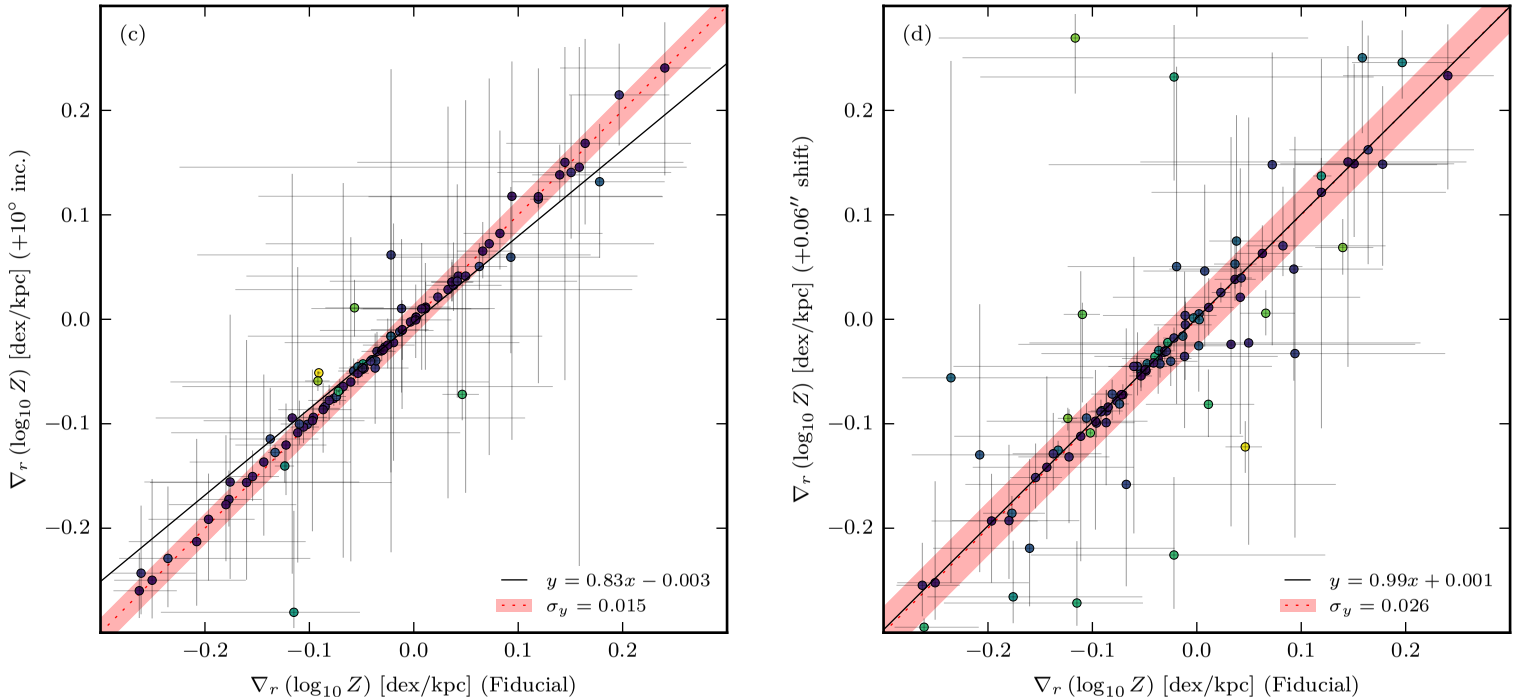

Figure 4.4: Sensitivity analysis of model inputs. On the horizontal axes we plot the metallicity gradients derived from our fiducial model. On the vertical axes we compare the metallicity gradients derived from the same data, but with the alternate model. The alternative models are identical to the fiducial except for one fixed parameter that has been adjusted slightly (see text for details). A different alternative model is plotted in each of the four panels, showing the effects of: (a) the width of metallicity gradient prior, (b) a misestimation of the PSF, (c) a miscalculation of the inclination and (d) misidentification of the galaxy centre. The errorbars show the $\pm 1\sigma$ quantiles of the metallicity gradient posterior probability distribution. Note that the errors of the two models are not independent and are likely to be highly correlated, consequently the errors appear much larger than the scatter. Each data point is coloured by the Jensen–Shannon distance between the 1D marginal posteriors of the fiducial and alternate models. In each panel a solid black line shows the best fit to the data (weighted by the inverse of the formal data errors). We show the 1:1 relation as a red dotted line. A red shaded region a indicates the (weighted) vertical scatter about this 1:1 relation. Equations for the best fit and scatter are given in the bottom-right corner of each panel. N.B. the errors between the fiducial and alternative models are likely to be highly correlated.

3.3.4 Sensitivity to galaxy centre misidentification

Finally, we address the impact of misidentifying the centre of the galaxy (the point about which the radial metallicity profile is defined). To explore this we re-analyse the data, but shift the galaxy centre 0.06″ along the direction of the galaxy's major axis. This distance is approximately one tenth the size of the MUSE's PSF. However, we remind the reader that the galaxy centre is actually defined from higher-resolution HST imaging. While an absolute 0.06″ shift will impact the smallest galaxies in our sample the most, it is arguable, however, that it is easier to define the centre of small compact galaxies than it is to define the centre of large irregular galaxy.

If galaxies have a radial metallicity profile, we might naïvely expect that shifting away from the true centre would result in a flatter metallicity gradient. However, in Fig. 4.4(d) we see no systematic trend towards flatter metallicity gradients. Misidentifying the galaxy centre appears to add no systematic bias, but it could add moderate scatter to the inferred metallicity gradients. We estimate this additional uncertainty to be ≈ 0.04 dex/kpc. We stress, as with the other results above, that these are only estimates of the additional uncertainty.

4 Results

In this section we study the metallicity gradients of our galaxies and search for trends with galaxy size, mass and SFR. Our main findings are as follows:

- We find that the average galaxy in our sample has a negative metallicity gradient. But, there is considerable scatter about this and a few galaxies have positive metallicity gradients.
- If we select the largest galaxies ($r_d > 3$ kpc) in our sample we find this scatter reduces. In fact there are no large galaxies with inverted metallicity gradients.
- We do not find significant trends between a galaxy's metallicity gradient and either its mass or its SFR. The lack of correlation with SFR is in contrast with other studies.

From our MUSE observations we have constructed a sample of 94 galaxies between $0.08 < z < 0.84$. At a 2σ significance level we identify 37 galaxies with negative metallicity gradients and 9 with positive gradients. We classify 26 galaxies having metallicity gradients that is consistent with zero gradient. Herein we shall term these galaxies as having flat metallicity gradients, a name which should not be over-interpreted; we do not claim galaxies with flat metallicity gradients to have no metallicity gradient, instead it is our analysis that may lack the statistical power to discriminate. A further 22 galaxies are flagged as unreliable for being sensitive to the metallicity gradient prior (Section 3.3.1). In Fig. 4.8 we provide an image atlas of the galaxies, wherein we indicate the metallicity gradient classification of each galaxies.

Our first result is that on average our galaxies have a negative metallicity gradient with a median of $-0.043^{+0.009}_{-0.007}$ dex/kpc (using bootstrap and Monte Carlo resampling). We also apply a Wilcoxon signed-rank test and reject the null hypothesis that the average metallicity gradient is zero ($p = 0.0013$). This contrasts with the findings of Wuyts et al. (2016) in their study of $0.6 \lesssim z \lesssim 2.6$ galaxies they find an average metallicity gradient that is flat.

In Fig. 4.5 we present the metallicity gradients of galaxies against their size. Panels (a & b) show the metallicity gradient expressed in both scaled units (dex/r_d) and physical units (dex/kpc), respectively. Throughout the remainder of this work we will present metallicity gradient in scaled units that normalize for the galaxy's size. At low redshift there is growing consensus that when expressed this way, isolated massive galaxies ($\gtrsim 10^8$ M$_\odot$) share a common

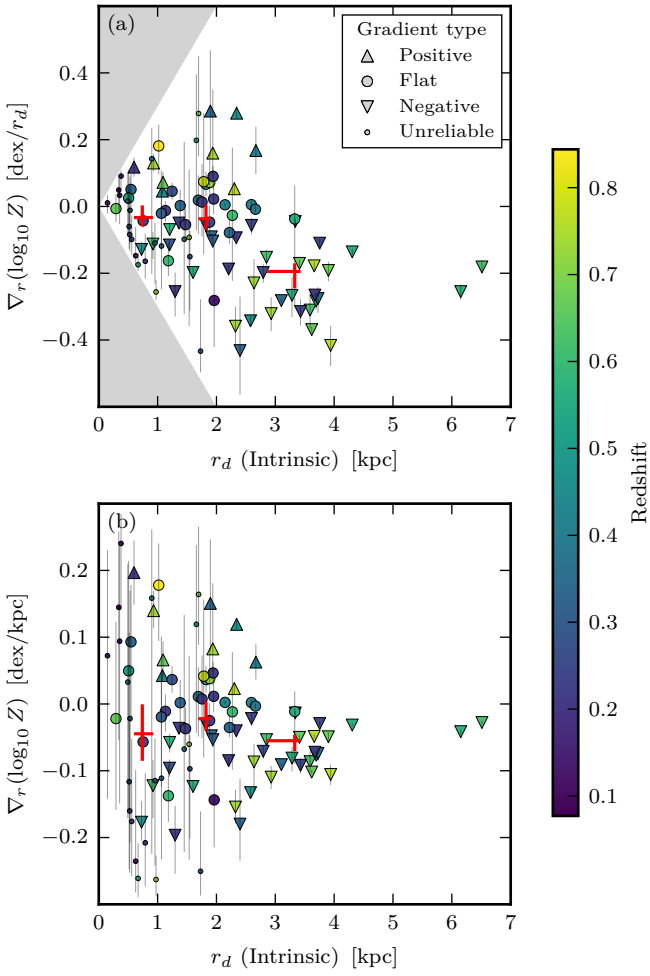

Figure 4.5: Metallicity gradients of galaxies as a function of their size. On the horizontal axes we plot the disc scale-length of the galaxies. On the vertical axes we show the metallicity gradient. In (a) we have normalized the metallicity gradient to the disc scale-length, while in (b) we display the same data but with the metallicity gradient expressed in physical units. Symbols indicate our metallicity gradient classification: triangles pointing up/down are galaxies with 2σ positive/negative gradients, large circles represent galaxies that have metallicity gradients consistent flat, and small circles indicate galaxies flagged for their sensitivity to the prior (the squares in Fig. 4.4(a)). Data points are coloured according to the galaxy's redshift. We overplot three red crosses, which indicate the median trend of the metallicity gradient with size. Errors on the median are determined by bootstrapping the sample, and Monte Carlo sampling of the errors (this includes unreliable galaxies). In (a) a portion of the plot is shaded grey, this denotes a region that is disallowed by our prior on the metallicity gradient.

Table 4.3: Analysis of unexplained (intrinsic) scatter in the metallicity gradients. We model the metallicity gradients as if they were normally distributed with mean, μ, and standard deviation, $\sigma_{\rm int}$. The galaxies are divided into two groups: those smaller, and those larger than $r_d = 0.3$. We show results for metallicity gradients expressed in both physical units (dex/kpc) and scaled units (dex/r_d). The unreliable galaxies, which are sensitive to the prior, are not included in this analysis. Including them would not significantly alter the results.

Gradient units	Size	μ	$\sigma_{\rm int}$	# of galaxies
dex/kpc	≤ 3 kpc	$-0.023^{+0.012}_{-0.012}$	$0.080^{+0.011}_{-0.009}$	54
	> 3 kpc	$-0.062^{+0.008}_{-0.008}$	$0.031^{+0.008}_{-0.005}$	18
dex/r_d	≤ 3 kpc	$-0.043^{+0.019}_{-0.020}$	$0.134^{+0.017}_{-0.015}$	54
	> 3 kpc	$-0.232^{+0.023}_{-0.025}$	$0.099^{+0.025}_{-0.018}$	18

value for the metallicity gradient (Sánchez et al. 2014; Ho et al. 2015). While this may not be true at higher redshift, we will nonetheless use scaled units.

From Fig. 4.5 it is clear that the average galaxy has a negative metallicity gradient. However, it is also clear that there is considerable scatter. There is a noticeable trend for the median metallicity gradient to become more negative with increasing galaxy size. We see that amongst the large galaxies ($\gtrsim 3$ kpc) there are no galaxies with positive metallicity gradients. Indeed almost all large galaxies have negative metallicity gradients. Conversely, the small galaxies ($\lesssim 3$ kpc) present a range of metallicity gradients, some negative and some positive.

The scatter in the metallicity gradient appears to sharply increase below $\lesssim 3$ kpc. However, we see that the errorbars of the small galaxies also increase. It is therefore important to ask whether there is a true increase in the *intrinsic* scatter in the small galaxies. In Table 4.3 we present an analysis of the amount of intrinsic scatter in both the small and large galaxies. For this we model the metallicity gradients if they were normally distributed with mean, μ, and standard deviation, $\sigma_{\rm int}$. This analysis accounts for the full posterior distributions on the metallicity gradient. We see that there is indeed an increase in the intrinsic scatter in the small galaxies ($\lesssim 3$ kpc) and that the mean is overall negative.

However, we caution that although we call this intrinsic scatter, it is perhaps more honest to call it unexplained scatter. It could simply be that our model is underestimating the true error in the metallicity gradient. Indeed it is somewhat suspicious that we see an increase in the scatter towards the smaller galaxies. We naïvely would expect that the small galaxies to be more sensitive to model specification errors, i.e. errors in the PSF or inclination (see Section 3.3). Nevertheless the sharpness of increase in scatter is certainly worthy of note.

Given that we see the galaxies with positive metallicity gradients are exclusively small, we also might expect they are also less massive. However, this does not appear to be the case in Fig. 4.6(a) where we compare the metallicity gradients against the total stellar mass of the galaxy. Galaxies with positive metallicity gradients span a similar mass range to those with negative gradients. That said, it does appear that on average metallicity gradient decreases with increasing mass. However, because of our galaxy selection, it is hard to interpret this. With a larger sample one might be disentangle the coupled selection effects on mass, size and redshift.

It is easier, however, to discuss the more massive portion of our sample. For example, at masses above $\approx 10^9\,{\rm M}_\odot$ we notice there is a large range of metallicity gradients, with hints that the scatter is perhaps greater in the higher-redshift galaxies. This certainly is in direct contrast to the low-redshift result of a common metallicity gradient. This discrepancy might be resolved if many of these galaxies are not isolated, but are instead interacting with other

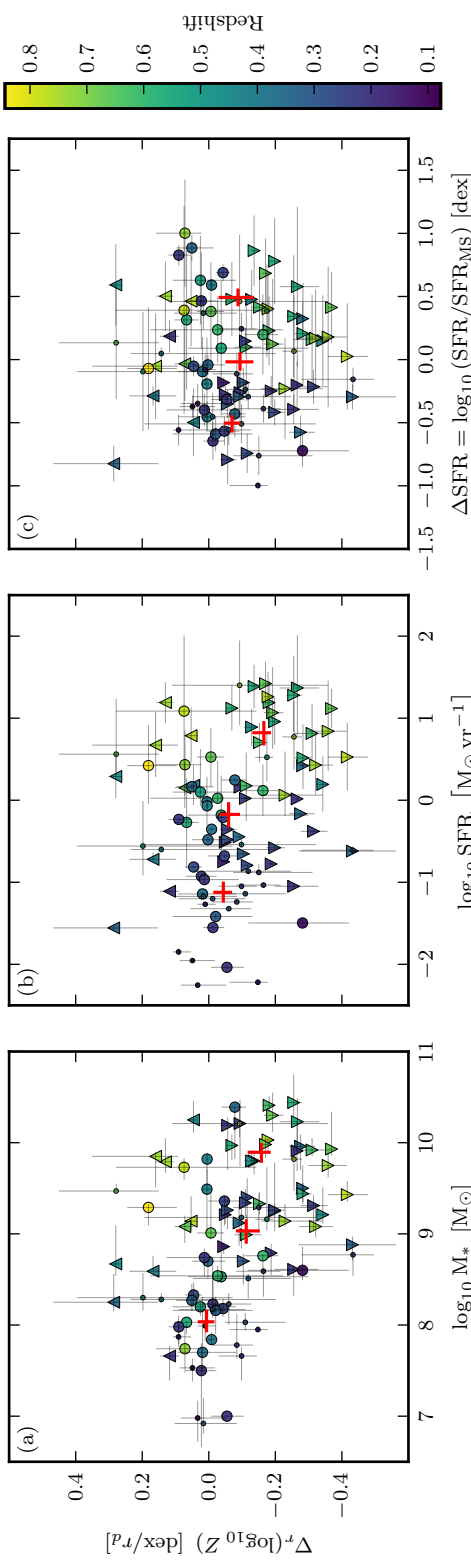

Figure 4.6: Metallicity gradients of galaxies as a function of their: stellar mass, star formation rate, and ΔSFR (the SFR of a galaxy relative to what would expected for a galaxy on the main-sequence with identical mass and redshift). These are shown in panels (a), (b) and (c) respectively. See Fig. 4.5 for a full description of plot (symbols, colours etc.). In panel (c) we have used the main-sequence parametrization of Whitaker et al. (2012).

galaxies. Because interacting galaxies typically have flatter metallicity gradients than would otherwise be expected (Rich et al. 2012).

Since interactions could trigger increased star-formation rates in interacting galaxies, Stott et al. (2014) suggested that the scatter in the observed metallicity gradients could be explained by the SFR. In Fig. 4.6(b) we compare the metallicity gradient to the SFR, however, we do not observe a trend towards more positive metallicity at high SFRs. Admittedly the association between interacting galaxies and higher SFR might be probably weak. However, in fact we see a slight trend in the opposite direction more negative gradients at high-SFRs. We caution that this trend could be a manifestation of our sample selection. Notably the SFR of a galaxy in our sample correlates with its redshift. This is in part because at higher redshifts we are biased towards the brighter, more strongly star-forming galaxies. But, it is also in part because the galaxy main-sequence has evolved, and the average SFR has decreased since $z \approx 1$.

So, to put galaxies on an even footing, we normalize the SFR relative to the main sequence. We define the main-sequence offset, ΔSFR, as the difference between a galaxy's SFR and the SFR of a galaxy on the main sequence which has identical mass and redshift, where we take the parametrisation of the main sequence evolution from Whitaker et al. (2012). In Fig. 4.6(c) we show the metallicity gradients of our galaxies against ΔSFR. We see that the trend towards negative gradients with increasing SFR now disappears. In fact in this projection, there appears to be no trends whatsoever. The average gradient is more or less constant, and there is large scatter irrespective of a galaxy's position relative to the main-sequence.

This is in contrast to the results of Stott et al. (2014) who find a positive correlation between specific star-formation rate (sSFR) and metallicity gradient. They find galaxies that are vigorously forming stars have flatter or even positive gradients. The authors suggest that an event causing infall of metal-poor gas would simultaneously trigger intense star-formation and reduce the central metallicity (thus flattening or inverting the metallicity profile). Our findings challenge such a simplistic explanation for the cause of inverted metallicity gradients. However, our results do not automatically preclude the mechanisms of galaxy–galaxy interactions and/or cold flows for triggering star-formation.

In the next section we shall discuss our results in more detail, placing them in context with other observations and theoretical work.

5 Discussion

5.1 Literature comparison

The work we present here is the first large systematic study of metallicity gradients in galaxies between $0.1 \lesssim z \lesssim 0.8$. However, there have been numerous studies of metallicity gradients in galaxies at lower and higher redshifts. In Fig. 4.7(a) we plot our results alongside several of these studies. Many of the high-redshift observations have used IFS techniques similar to ours, although some use observations of gravitationally lensed galaxies. Ideally these lensed observations will have sufficient resolution that seeing does not significantly affect the observed metallicity gradient. Therefore it is worth of note that both the lensed and non-lensed studies are consistent with one another, both having means centred around zero. And, apart from some lensed galaxies with very steep negative metallicity gradients, the scatter of the two are similar.

There is, however, a notable discontinuity between our observations and the other studies at $0.8 \lesssim z \lesssim 2.6$. This transition is most visible in the increased scatter of our observations. But there is also a shift in the average gradient to slightly negative gradients. While these effects could be attributed to the real evolution of metallicity gradients with cosmic time, the sharpness of the discontinuity would argue for a less-astrophysical causes.

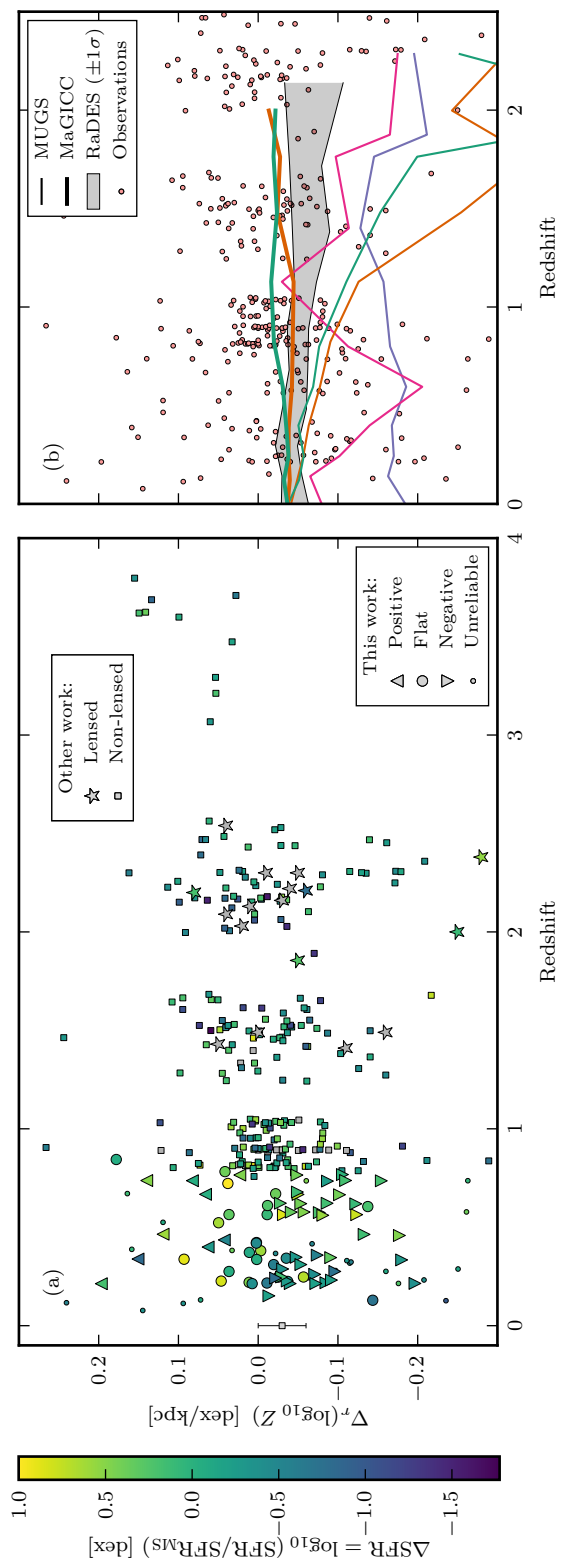

Figure 4.7: Comparison of our results with other literature, including both numerical simulation and observations. (Left) We show observational results (ours and others) compared with various numerical simulations that are overplotted. The grey shaded region indicated the $\pm 1\sigma$ spread of metallicity gradients from 19 RaDES galaxies (Few et al. 2012). Thin coloured lines indicate MUGS galaxies (Stinson et al. 2010). Two of these galaxies (the orange and green lines) were re-simulated with in the MaGGIC simulations (Gibson et al. 2013) and are shown as thick orange/green lines. (Right) We compare our observational results against other studies. These metallicity gradients come from studies of galaxies that have been gravitationally lensed (star symbols), and non-lenses galaxies (squares). Where possible we colour data points to indicate the SFR relative the the main sequence (ΔSFR). The $z \approx 0$ data point represents the mean and scatter in metallicity gradients reported in Sánchez et al. (2014). We compile lensing results from Yuan et al. (2011), Jones et al. (2013), Jones et al. (2015), Leethochawalit et al. (2016) and Wang et al. (2017). The non-lensed results are gathered from Queyrel et al. (2012), Swinbank et al. (2012), Stott et al. (2014), Troncoso et al. (2014) and Wuyts et al. (2016).

There are a few plausible explanations. Of which the most concerning for us is that this could highlight an issue with our method for determining metallicity gradients. A systematic overcompensation for seeing effects certainly could produce steeper gradients. It is harder, however, to conceive of systematic effects that would produce a shift away from a non-zero average gradient. In support of our results, a slightly negative average gradient is in fact consistent with observations in the low-redshift universe (e.g. Sánchez et al. 2014).

There is another reason that we might see this discontinuity between the observational studies. The vast majority the $0.8 \lesssim z \lesssim 2.6$ galaxies have metallicity gradients determined using the N2 ratio ([N II]6584/Hα). Whereas we use a very different method for deriving metallicity. It is well known that there are large discrepancies between different metallicity determination methods (Kewley & Ellison 2008). The particular N2 calibration used in the other studies may produce metallicity gradients that are systematically flatter than our method.

An advantage of our method is that it produces a self-consistent metallicity gradient analysis, independent of the available emission-lines. With our MUSE observations we lose emission-lines redward of Hα at $z \gtrsim 0.4$. However, we do not observe a systematic shift in our measurements at $z \approx 0.4$, suggesting that our method is indeed self-consistent.

On a related note it is questionable whether any of these metallicity methods are valid at high redshift, since most metallicity calibrations and photoionization models are designed for low-redshift interstellar medium (ISM) conditions. For example, it is generally accepted that the electron density of the ISM was higher at earlier times (Shirazi et al. 2014; Sanders et al. 2016), but the D13 photoionization models we use are computed only at low densities ($\approx 10\,\mathrm{cm}^{-3}$). Beyond changes in density, there lack of consensus whether other conditions have changed. At earlier times the ionization parameter, hardness of the ionizing spectrum, or nitrogen-to-oxygen abundance ratio may have been different, although there is little consensus (e.g. Onodera et al. 2016; Kashino et al. 2017; Steidel et al. 2016, and references therein). Our method is certainly not immune to these issues, however, since our observations are all below $z \approx 0.8$ it may not be so incredible to apply the same assumptions that we use at low-redshift. It is worth noting that, because we marginalize over galaxy wide variations in the ionization parameter, our method may partially mitigate against some of the variations in ISM conditions. Because, to first order the largest variations in nebular emission-line spectra are typically due to metallicity and ionization-parameter (Dopita et al. 2000).

5.2 Interpretation

In the work presented here we find on average galaxies between $0.1 \lesssim z \lesssim 0.8$ have a negative metallicity gradient. However, there is considerable scatter about this, with some galaxies exhibiting a positive metallicity gradient. As reported by Pilkington et al. (2012), at any given redshift the numerical simulations predict that there is intrinsic scatter in the metallicity gradient. This can be seen in Fig. 4.7(b) when comparing the scatter *within* the MUGS galaxies (Stinson et al. 2010) and within the RaDES galaxies (Few et al. 2012). One should note that the difference *between* the MUGS and RaDES simulations are, however, attributable to differences in the numerical recipes for star-formation and feedback in the various simulations. Flatter metallicity gradients arise from the model prescriptions with more intense feedback. For example the MaGICC simulations (Gibson et al. 2013) re-simulate two of the MUGS galaxies using an enhanced feedback recipe. The increased feedback produces galaxies with metallicity gradients that are consistently flatter at all redshifts. Gibson et al. (2013) attribute this to central gas being lost in outflows that is later recycled back into the galaxy, but at larger radii.

The intrinsic diversity in metallicity gradients that we observe (also mirrored in the simulations) would indicate that at earlier times there is no common metallicity gradient. It is perhaps surprising that we observe a common abundance gradient in the universe today. That said, as

we shall later suggest, this contradiction is not necessary as acute as it would first appear. A common metallicity gradient may only exist in large galaxies.

Even though simulations can produce a large range of metallicity gradients, they typically do not reproduce the same inverted metallicity gradients that we and others observe. Simulations tend to produce galaxies with negative metallicity gradients (both steep and shallow). Some of these simulations have next to no redshift dependence, while others suggest the metallicity gradient was steeper at earlier times. Despite this variety, simulations never produce galaxies with positive metallicity gradients. Indeed, with the classical understanding of inside-out growth one expects negative metallicity gradients (Portinari & Chiosi 1999). Radial mixing of gas could flatten the metallicity gradient, but it is hard to conceive of secular processes that could produce positive metallicity gradients.

Consistent with other higher redshift studies we identify a small fraction of our galaxies that have significantly positive metallicity gradients. Contrast this with galaxies at much high-redshift ($z \approx 3.4$) where all galaxies have galaxy centres are systematically more metal poor than their outskirts (Troncoso et al. 2014). In related work, Cresci et al. (2010) attribute this metallicity gradient inversion to cold flows (e.g. Dekel et al. 2009). Cold flows are streams of cold gas that penetrate the hot galaxy halo and fuel star formation in galaxies. It is argued that if this metal-poor cold gas can reach the innermost regions of a galaxy (the deepest part of the gravitational potential) then this would explain the metallicity gradient inversion.

It should be noted that cold flows are not the only way to transport metal-poor gas inner portions of a galaxy. As suggested by Rich et al. (2012) galaxy–galaxy interactions could cause radial inflow of gas though the galaxy's disc. Metal-poor gas from the outskirts is therefore deposited in the galaxy centre. Simulations of Rupke et al. (2010) and Torrey et al. (2012) find that interacting galaxies have flat (but not positive) metallicity gradients. Is not clear whether galaxy interactions could truly invert the metallicity gradient.

In contrast to the inflow mechanisms above, outflows could also provide an alternative explanation for positive metallicity gradients. Intense centrally-concentrated star formation could produce significant outflows that entrain metal-rich gas. Using simple analytical chemical evolution arguments Cresci et al. (2010) disfavoured a wind scenario as it would require mass outflow rates far in excess of the observed SFR. That said, Troncoso et al. (2014) point out that if this metal-rich gas falls back preferentially onto the outer regions of the galaxy, it could raise the outer metallicity. This "fountaining" could then enhance the ability of winds to produce positive metallicity gradients and hence reduce the required outflow rates down to more realistic levels.

Of course, the inflow and outflow scenarios need not be mutually exclusive. Gas accretion could trigger intense star formation that drives the winds. In either case (inflows and/or outflows) we should expect to observe elevated star-formation rates. In support of this Stott et al. (2014) and Wuyts et al. (2016) find weak correlations between the specific star-formation rate (sSFR) and metallicity gradient (galaxies with more intense star-formation have flatter or even positive metallicity gradients). In contrast, we do not find systematically different metallicity gradients in galaxies with elevated SFR (Fig. 4.6(c)). A difference in the sample selection might plausibly account for the difference between our results and previous studies. Alternatively one should also consider that, if the intense star-formation is confined to a galaxy's centre, the *global* SFRs of a galaxy may not be a very sensitive indicator of inflow or outflow events.

There is perhaps another way to reconcile the lack of correlation between metallicity gradient and star-formation intensity. Contrary to our earlier assertion, it has been recently proposed by Schönrich & McMillan (2017) that inverted metallicity gradients can actually arise mostly within the framework of secular inside-out growth. This is achieved in conjunction

with outflows that recycle enriched gas from the galaxy centre, transporting to larger radii. Schönrich & McMillan (2017), however, show that these positive metallicity gradients do not persist throughout a galaxies life, and in fact are only expected to exist at early times in a galaxy's evolution. Unfortunately, given the large number of model uncertainties, they are unable to make rigorous predictions for how long this phase may last.

We find the results of Schönrich & McMillan (2017) intriguing as they may shed light on another curious result of our study. In the small galaxies ($r_d < 3$ kpc) we observe a large scatter of the metallicity gradient, whilst larger galaxies present negative metallicity gradients with minimal scatter. If the smaller galaxies are comparatively less evolved systems, then this secular evolution (with metallicity gradient inversion at early times) may account for the diversity of metallicity gradients observed. Consequently the larger galaxies, with their negative metallicity gradients, would be emblematic of the more classical understanding of inside-out growth which produces a common metallicity gradient (e.g. Prantzos & Boissier 2000). This would reconcile our results with the low-redshift universe. And as such we could expect to find inverted metallicity gradients in small galaxies today.

6 Conclusions

Using MUSE GTO data we present metallicity gradients for a sample of 94 intermediate redshift galaxies ($0.1 \lesssim z \lesssim 0.8$). By applying a forward-modelling technique we are able to infer the true metallicity gradient, correcting for seeing effects. We compare the observed metallicity gradient against global properties such as galaxy mass, size and SFR. From this we conclude the following:

- We find the average galaxy in our sample has a negative metallicity gradient. Nevertheless there is significant scatter and we classify 9 of the 94 galaxies as having positive metallicity gradients.
- We do not identify any significant correlation of the metallicity gradient with either total SFR or stellar mass. And we find no correlation whatsoever once the SFR is normalized relative to the main sequence.
- This lack of correlation in the latter runs contrary to previous studies. These studies, predominantly at higher redshifts ($0.6 \lesssim z \lesssim 2.6$), cited such a correlation as being suggestive of sudden inflow or merger events that might trigger star-formation while simultaneously flattening/inverting the metallicity gradient. Our results, however, do not support this interpretation at the intermediate redshifts we study.
- The largest galaxies in our sample ($r_d > 3$ kpc) are found to have almost exclusively negative metallicity gradients. On the contrary, the smaller galaxies ($r_d < 3$ kpc) present a range of metallicity gradients. The small galaxies exhibit a larger intrinsic scatter in the metallicity gradient.
- We liken the large galaxies as similar to galaxies observed in the universe today, where galaxies present a common metallicity gradient. In addition we speculate that the size dichotomy may be related to a secular understanding of inside-out growth, where a common metallicity gradient is only established in large (well-evolved) systems.
- However, we advise caution on this last point. Intrinsically smaller galaxies are also more affected by seeing-induced resolution loss. Therefore for these small galaxies our inferred metallicity gradients (and their errors) are presumably more dependent on the accuracy of our modelling (see Section 3.3).

The MUSE GTO surveys are currently ongoing and in the future we will provide us with a larger sample of metallicity gradients. This data will allow us to separate potential selection effects and biases, which, in turn, will enable us at affirm our results.

In the future we will also study metallicity gradients in conjunction with gas kinematics of the galaxies. By also quantifying the local environments of our galaxies, we can study the impact of galaxy–galaxy interactions on the metallicity gradient, without relying on SFR as an indirect tracer.

Acknowledgements

JB acknowledges support from FCT grant IF/01654/2014/CP1215/CT0003.

Additionally we wish to acknowledge both the PYTHON programming language and the Interactive Data Language (IDL) that were both used extensively throughout this work.

Bibliography

Abraham R. G., et al., 2007, ApJ, 669, 184
Bacon R., et al., 2010, in Ground-based and Airborne Instrumentation for Astronomy III. p. 773508, doi:10.1117/12.856027
Bacon R., et al., 2015, A&A, 575, A75
Baldry I. K., et al., 2014, MNRAS, 441, 2440
Baldwin J. A., Phillips M. M., Terlevich R., 1981, PASP, 93, 5
Bertin E., Arnouts S., 1996, A&AS, 117, 393
Bresolin F., Kennicutt R. C., Ryan-Weber E., 2012, ApJ, 750, 122
Brinchmann J., Charlot S., White S. D. M., Tremonti C., Kauffmann G., Heckman T., Brinkmann J., 2004, MNRAS, 351, 1151
Brinchmann J., Charlot S., Kauffmann G., Heckman T., White S. D. M., Tremonti C., 2013, MNRAS, 432, 2112
Bruzual G., Charlot S., 2003, MNRAS, 344, 1000
Buchner J., et al., 2014, A&A, 564, A125
Calzetti D., Armus L., Bohlin R. C., Kinney A. L., Koornneef J., Storchi-Bergmann T., 2000, ApJ, 533, 682
Capak P., et al., 2007, ApJS, 172, 99
Carton D., et al., 2015, MNRAS, 451, 210
Carton D., et al., 2017, MNRAS, 468, 2140
Casertano S., et al., 2000, AJ, 120, 2747
Chabrier G., 2003, PASP, 115, 763
Charlot S., Fall S. M., 2000, ApJ, 539, 718
Contini T., et al., 2016, A&A, 591, A49
Cresci G., Mannucci F., Maiolino R., Marconi A., Gnerucci A., Magrini L., 2010, Nature, 467, 811
Danovich M., Dekel A., Hahn O., Ceverino D., Primack J., 2015, MNRAS, 449, 2087
Dekel A., Birnboim Y., 2006, MNRAS, 368, 2
Dekel A., et al., 2009, Nature, 457, 451
Dopita M. A., Sutherland R. S., 2003, Astrophysics of the diffuse universe
Dopita M. A., Kewley L. J., Heisler C. A., Sutherland R. S., 2000, ApJ, 542, 224
Dopita M. A., Sutherland R. S., Nicholls D. C., Kewley L. J., Vogt F. P. A., 2013, ApJS, 208, 10

Feroz F., Hobson M. P., 2008, MNRAS, 384, 449
Feroz F., Hobson M. P., Bridges M., 2009, MNRAS, 398, 1601
Feroz F., Hobson M. P., Cameron E., Pettitt A. N., 2013, preprint, (arXiv:1306.2144)
Few C. G., Gibson B. K., Courty S., Michel-Dansac L., Brook C. B., Stinson G. S., 2012, A&A, 547, A63
Gibson B. K., Pilkington K., Brook C. B., Stinson G. S., Bailin J., 2013, A&A, 554, A47
Guo Y., et al., 2013, ApJS, 207, 24
Hao C.-N., Kennicutt R. C., Johnson B. D., Calzetti D., Dale D. A., Moustakas J., 2011, ApJ, 741, 124
Ho I.-T., Kudritzki R.-P., Kewley L. J., Zahid H. J., Dopita M. A., Bresolin F., Rupke D. S. N., 2015, MNRAS, 448, 2030
Jones T., Ellis R. S., Richard J., Jullo E., 2013, ApJ, 765, 48
Jones T., et al., 2015, AJ, 149, 107
Juneau S., et al., 2014, ApJ, 788, 88
Kashino D., et al., 2017, ApJ, 835, 88
Kauffmann G., et al., 2003, MNRAS, 346, 1055
Kennicutt R. C., Evans N. J., 2012, ARA&A, 50, 531
Kereš D., Katz N., Weinberg D. H., Davé R., 2005, MNRAS, 363, 2
Kewley L. J., Ellison S. L., 2008, ApJ, 681, 1183
Kewley L. J., Dopita M. A., Sutherland R. S., Heisler C. A., Trevena J., 2001, ApJ, 556, 121
Knobel C., et al., 2012, ApJ, 753, 121
Kriek M., van Dokkum P. G., Labbé I., Franx M., Illingworth G. D., Marchesini D., Quadri R. F., 2009, ApJ, 700, 221
Larson R. B., 1976, MNRAS, 176, 31
Leethochawalit N., Jones T. A., Ellis R. S., Stark D. P., Richard J., Zitrin A., Auger M., 2016, ApJ, 820, 84
Luridiana V., Morisset C., Shaw R. A., 2015, A&A, 573, A42
Marino R. A., et al., 2016, A&A, 585, A47
Murphy E. J., et al., 2011, ApJ, 737, 67
Onodera M., et al., 2016, ApJ, 822, 42
Pilkington K., et al., 2012, A&A, 540, A56
Portinari L., Chiosi C., 1999, A&A, 350, 827
Prantzos N., Boissier S., 2000, MNRAS, 313, 338
Queyrel J., et al., 2012, A&A, 539, A93
Rafelski M., et al., 2015, AJ, 150, 31
Rich J. A., Torrey P., Kewley L. J., Dopita M. A., Rupke D. S. N., 2012, ApJ, 753, 5
Rosales-Ortega F. F., Díaz A. I., Kennicutt R. C., Sánchez S. F., 2011, MNRAS, 415, 2439
Rupke D. S. N., Kewley L. J., Barnes J. E., 2010, ApJ, 710, L156
Sánchez S. F., et al., 2014, A&A, 563, A49
Sanders R. L., et al., 2016, ApJ, 816, 23
Schönrich R., McMillan P. J., 2017, MNRAS,
Shirazi M., Brinchmann J., Rahmati A., 2014, ApJ, 787, 120
Soto K. T., Lilly S. J., Bacon R., Richard J., Conseil S., 2016, MNRAS, 458, 3210
Steidel C. C., Strom A. L., Pettini M., Rudie G. C., Reddy N. A., Trainor R. F., 2016, ApJ, 826, 159
Stewart K. R., Kaufmann T., Bullock J. S., Barton E. J., Maller A. H., Diemand J., Wadsley J., 2011, ApJ, 738, 39
Stinson G. S., Bailin J., Couchman H., Wadsley J., Shen S., Nickerson S., Brook C., Quinn T., 2010, MNRAS, 408, 812

Storey P. J., Hummer D. G., 1995, MNRAS, 272, 41
Stott J. P., et al., 2014, MNRAS, 443, 2695
Swinbank A. M., Sobral D., Smail I., Geach J. E., Best P. N., McCarthy I. G., Crain R. A., Theuns T., 2012, MNRAS, 426, 935
Tacconi L. J., et al., 2013, ApJ, 768, 74
Torrey P., Cox T. J., Kewley L., Hernquist L., 2012, ApJ, 746, 108
Tremonti C. A., et al., 2004, ApJ, 613, 898
Troncoso P., et al., 2014, A&A, 563, A58
Vila-Costas M. B., Edmunds M. G., 1992, MNRAS, 259, 121
Wang X., et al., 2017, ApJ, 837, 89
Weilbacher P. M., Streicher O., Urrutia T., Jarno A., Pécontal-Rousset A., Bacon R., Böhm P., 2012, in Software and Cyberinfrastructure for Astronomy II. p. 84510B, doi:10.1117/12.925114
Whitaker K. E., van Dokkum P. G., Brammer G., Franx M., 2012, ApJ, 754, L29
Woods R. M., Wadsley J., Couchman H. M. P., Stinson G., Shen S., 2014, MNRAS, 442, 732
Wuyts E., et al., 2016, ApJ, 827, 74
York D. G., et al., 2000, AJ, 120, 1579
Yuan T.-T., Kewley L. J., Swinbank A. M., Richard J., Livermore R. C., 2011, ApJ, 732, L14
Yuan T.-T., Kewley L. J., Rich J., 2013, ApJ, 767, 106
Zaritsky D., Kennicutt Jr. R. C., Huchra J. P., 1994, ApJ, 420, 87
van de Voort F., Schaye J., Booth C. M., Dalla Vecchia C., 2011, MNRAS, 415, 2782
van der Wel A., et al., 2012, ApJS, 203, 24
van der Wel A., et al., 2014, ApJ, 788, 28

Appendices

A Additional figures

In Fig. 4.8 we provide an HST image atlas of our final galaxy sample. With each cutout image we indicate the inferred metallicity gradient.

In Figs. 4.9 & 4.10 we provide example plots for inspecting the quality of the model fit. Similar plots for all galaxies are available online (https://doi.org/10.5281/zenodo.581221).

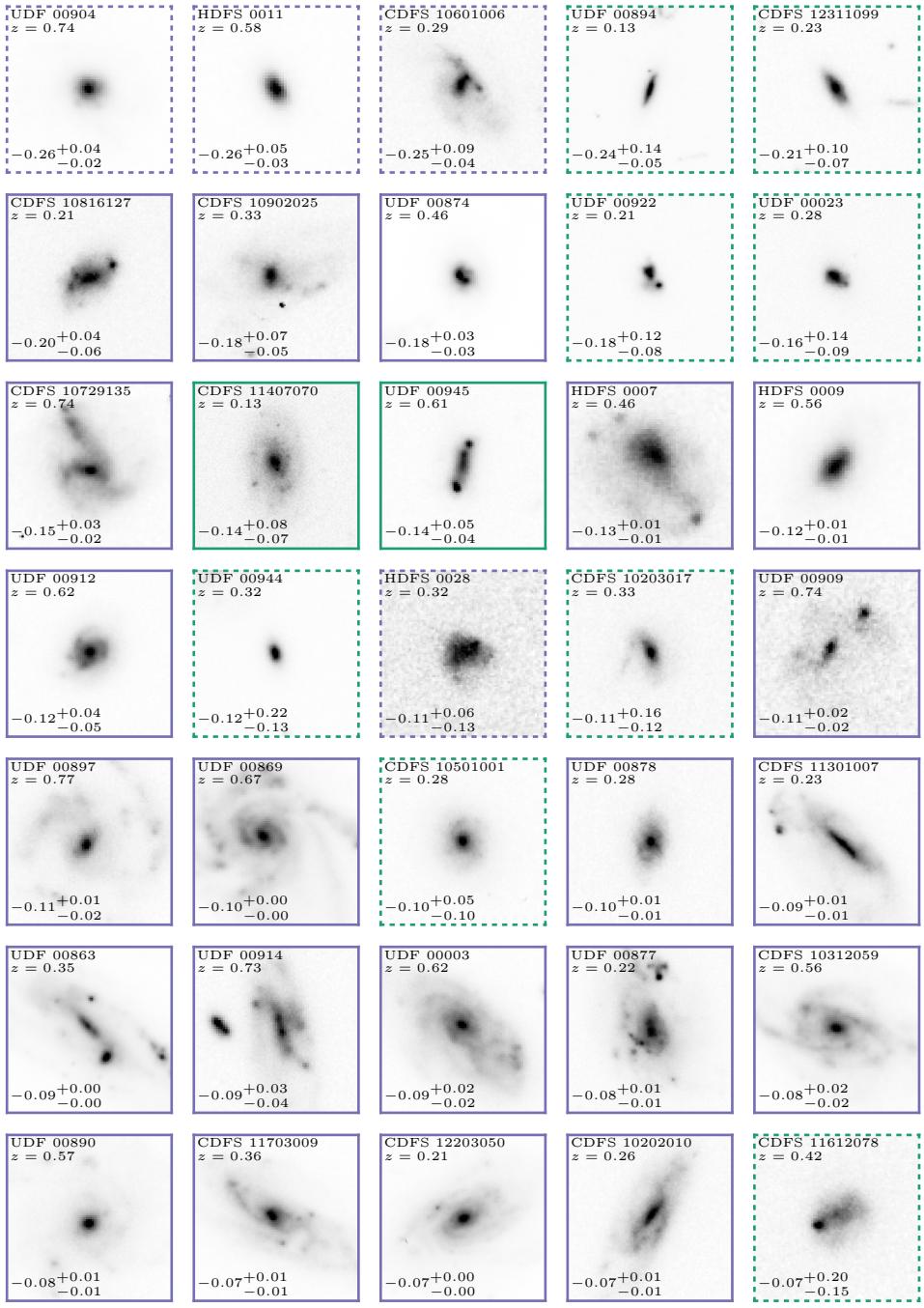

Figure 4.8: Image atlas showing cutouts of galaxies in our sample, shown in order of increasing metallicity gradient. Images are centred on the galaxy of interest, where North is up and East is left. The images are sized to be 16 kpc edge-to-edge. In the top-left corner of each panel we show the galaxy's redshift. In the bottom-left corner we display the inferred metallicity gradient (units are dex/kpc). The border colour displays the metallicity gradient type: negative gradients (blue), positive gradients (orange), flat gradients (green). Galaxies flagged as unreliable have dashed borders.

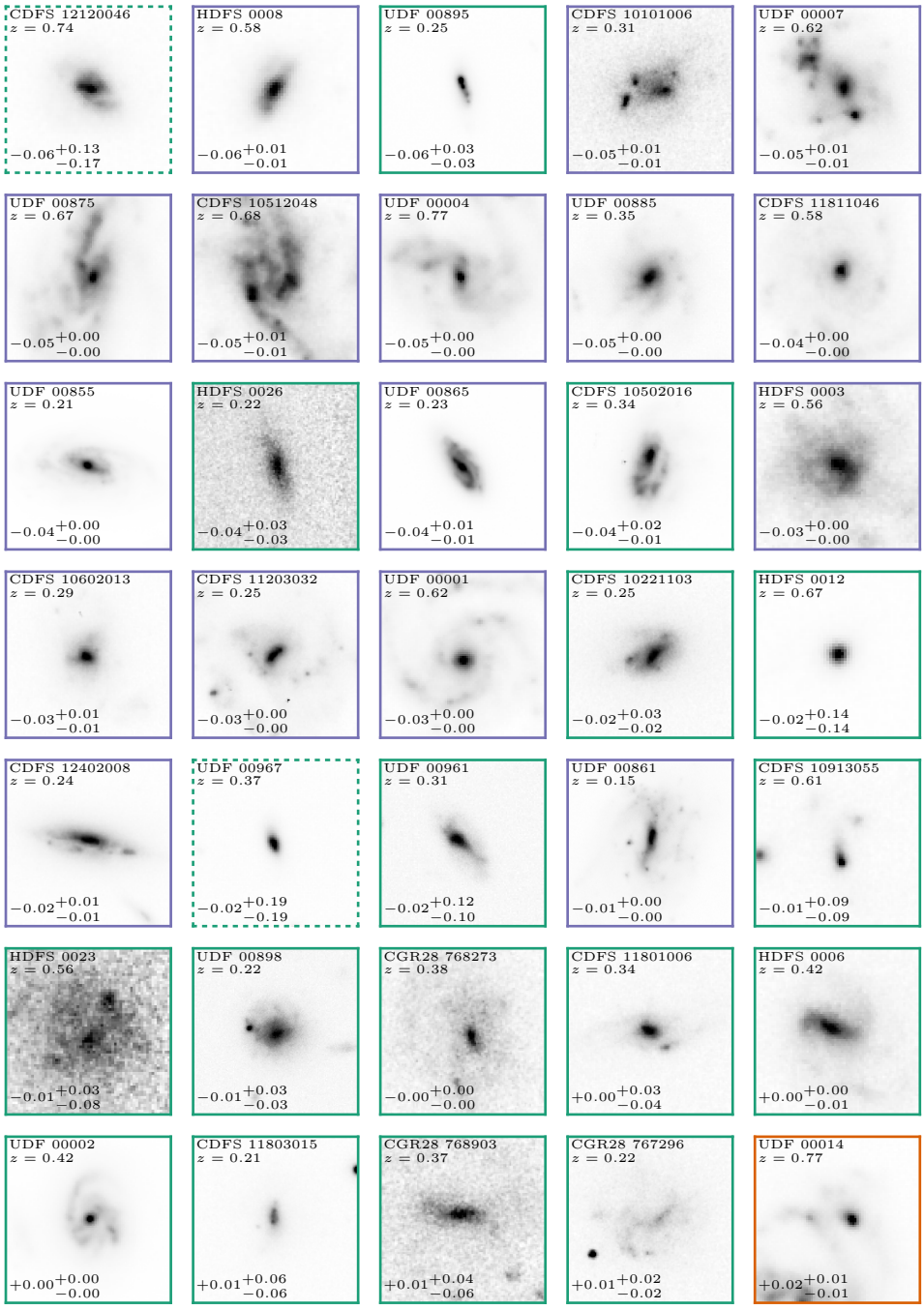

Figure 4.8 (*cont.*)

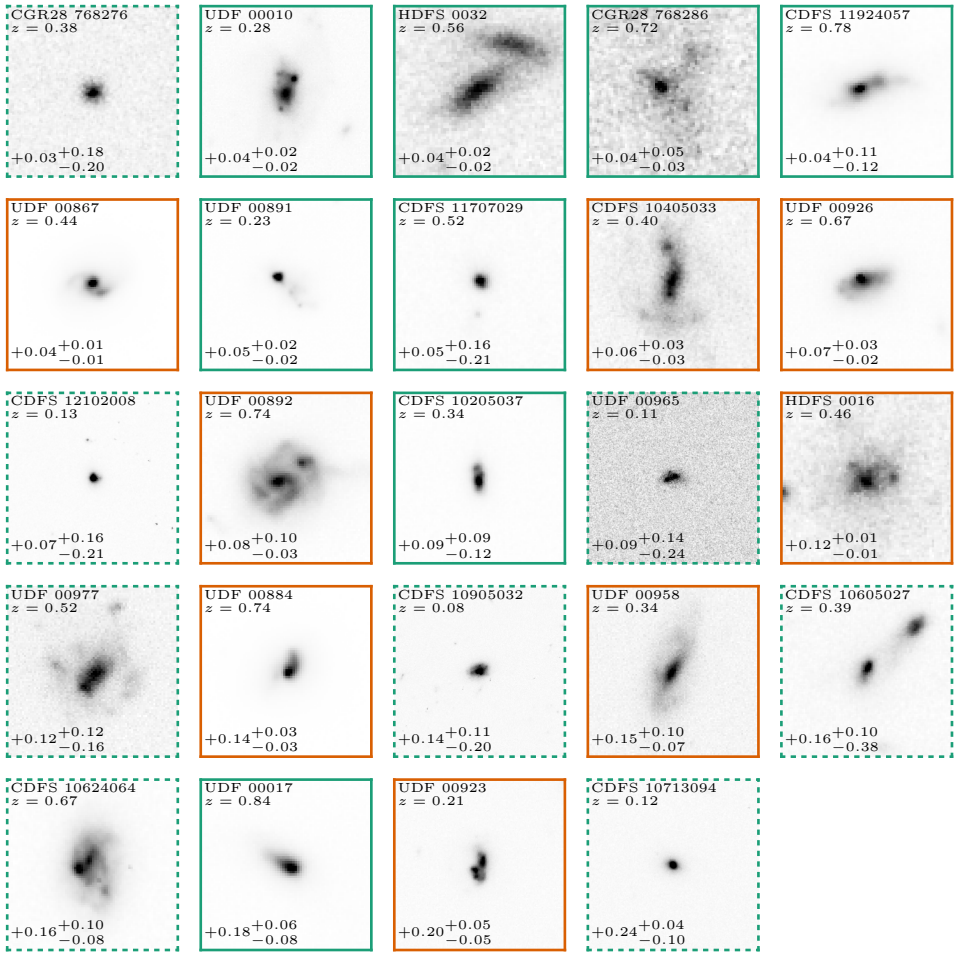

Figure 4.8 (*cont.*)

Figure 4.9: Visual quality assessment of model for galaxy HDFS-0003. This is an illustrative example and similar plots all galaxies can be found online. Top left: We show here the globally integrated MUSE spectrum. We also indicate the derived central metallicity, $\log_{10} Z_0$ in dex, and derived metallicity gradient, $\nabla_r (\log_{10} Z)$ in dex/kpc. Top right: We show the SFR map that was input into the modelling. A red cross indicate the galaxy centre. Left: We show the radial flux profiles for the modelled emission-lines. The name of the emission line is indicated in the top-right corner of each panel. An asterisk denotes lines that do not have observed fluxes in all spatial bins. Black data points indicate observed fluxes and their $\pm 1\sigma$ errors. The red crosses show the median model solution. The size of the vertical bar indicates a $\pm 2\sigma$ range in fluxes. Right: For each emission line we show three images. These are, respectively, the 2D binned images of the observed fluxes, model fluxes, and scaled residuals ($^{(\text{Observed} - \text{Model})}/_{\text{Error}}$) for each emission line. A black circle in the top-left corner represents the FWHM of the PSF. All images (including the SFR map) are shown on the same spatial scale. [For space, this plot has been truncated to show only {[O II], Hδ, Hγ, Hβ}. The full plot showing all lines (including also {[O III]4959, [O III]5007}) is available online.]

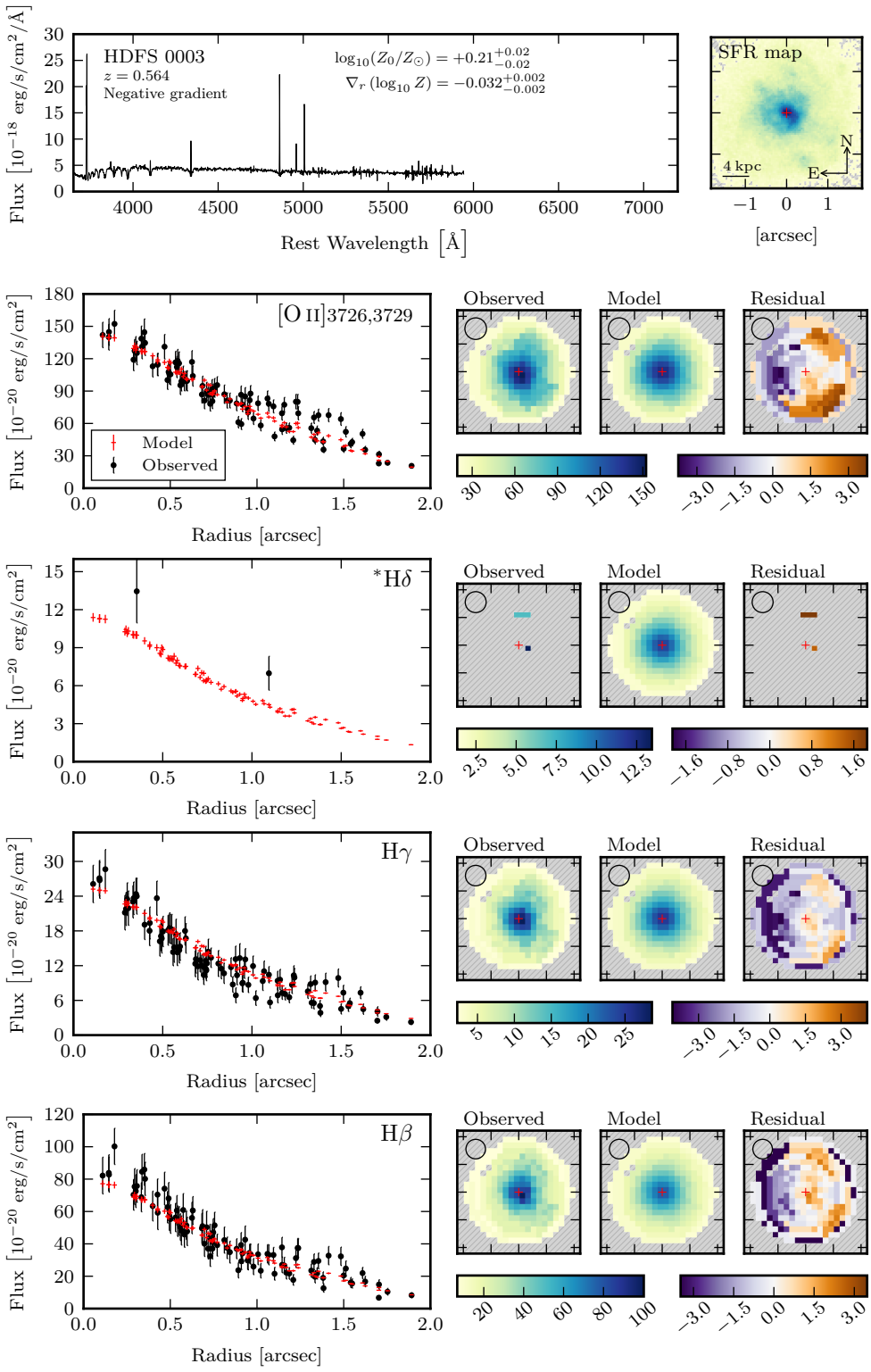

Figure 4.9 (*caption is shown on preceding page*)

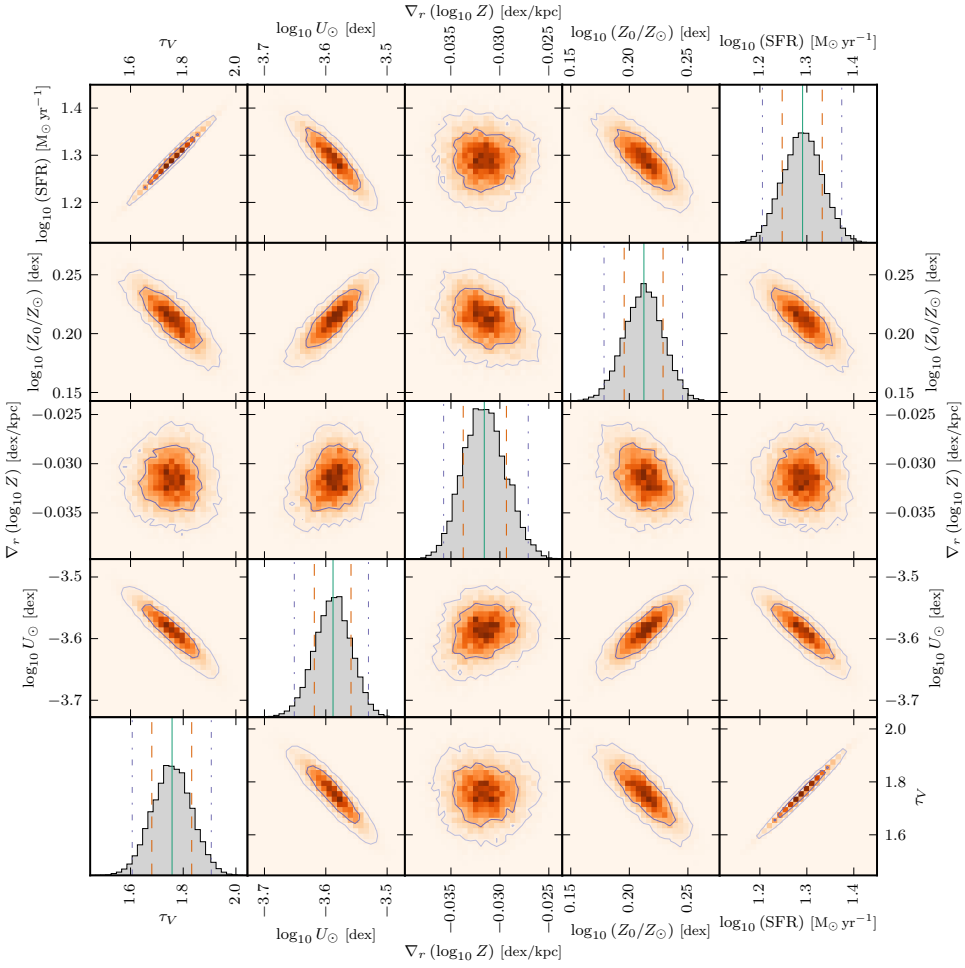

Figure 4.10: Plot showing derived model parameters for HDFS 0003. This is an illustrative example and similar plots all galaxies can be found online. We show both 1D and 2D marginalized histograms for all 5 parameters: the total star-formation rate, $\log_{10}(\mathrm{SFR})$, central metallicity, $\log_{10} Z_0$, metallicity gradient, $\nabla_r (\log_{10} Z)$, ionization parameter at solar metallicity, $\log_{10} U_\odot$, and V-band optical depth, τ_V. In each 1D histogram the vertical lines indicate the median (solid), $\pm 1\sigma$ quantiles (dashed) and $\pm 2\sigma$ quantiles (dash-dotted). In each 2D histogram we plot 1σ and 2σ contours. All axes span a $[-4\sigma, 4\sigma]$ interval in their respective parameters.